

Electronic structure and magnetism of $\text{Fe}_{3-x}\text{V}_x\text{X}$ ($\text{X} = \text{Si}, \text{Ga}$ and Al) alloys by the KKR-CPA method

A. Bansil

Department of Physics, Northeastern University, Boston, Massachusetts 02115

S. Kaprzyk

*Department of Physics, Northeastern University, Boston, Massachusetts 02115,
and*

*Faculty of Physics and Nuclear Techniques, Academy of Mining and Metallurgy,
al. Mickiewicza 30, 30-073 Kraków, Poland*

P.E. Mijnders

*Interfaculty Reactor Institute, Delft University of Technology,
Mekelweg 15, 2629 JB Delft, The Netherlands,
and*

Department of Physics, Northeastern University, Boston, Massachusetts 02115

J. Toboła

*Faculty of Physics and Nuclear Techniques, Academy of Mining and Metallurgy,
al. Mickiewicza 30, 30-073 Kraków, Poland*

(September 6, 2018)

Abstract

We present first principles charge- and spin-selfconsistent electronic structure computations on the Heusler-type disordered alloys $\text{Fe}_{3-x}\text{V}_x\text{X}$ for three different metalloids $\text{X}=(\text{Si}, \text{Ga} \text{ and } \text{Al})$. In these calculations we use the methodology based on the Korringa-Kohn-Rostoker formalism and the coherent-potential approximation (KKR-CPA), generalized to treat disorder in multi-component complex alloys. Exchange correlation effects are incorporated within the local spin density (LSD) approximation. Total energy calculations for $\text{Fe}_{3-x}\text{V}_x\text{Si}$ show that V substitutes preferentially on the Fe(B) site, not on the Fe(A,C) site, in agreement with experiment. Furthermore, calculations have been carried out for $\text{Fe}_{3-x}\text{V}_x\text{X}$ alloys (with, $x = 0.25, 0.50$ and 0.75), together with the end compounds Fe_3X and Fe_2VX , and the limiting cases of a single V impurity in Fe_3X and a single Fe(B) impurity in Fe_2VX . We delineate clearly how the electronic states and magnetic moments at various sites in $\text{Fe}_{3-x}\text{V}_x\text{X}$ evolve as a function of the V content and the

metalloid valence. Notably, the spectrum of $\text{Fe}_{3-x}\text{V}_x\text{X}$ ($\text{X}=\text{Al}$ and Ga) develops a pseudo-gap for the majority as well as minority spin states around the Fermi energy in the V-rich regime which, together with local moments of Fe(B) impurities, may play a role in the anomalous behavior of the transport properties. The total magnetic moment in $\text{Fe}_{3-x}\text{V}_x\text{Si}$ is found to decrease *non-linearly*, and the Fe(B) moment to *increase* with increasing x ; this is in contrast to expectations of the ‘local environment’ model, which holds that the total moment should vary linearly while the Fe(B) moment should remain constant. The common-band model which describes the formation of bonding and antibonding states with different weights on the different atoms, however, provides insight into the electronic structure of this class of compounds.

I. INTRODUCTION

Heusler-type ternary and pseudo-binary compounds¹ Y_2ZX in the $L2_1$ or DO_3 structure, where Y and Z denote metal atoms and X is a metalloid, display a remarkably rich variety of behavior in their electronic, magnetic and transport properties. Among early studies of the Fe-based alloys, a note may be made of the work on $FeAl$,²⁻⁴ $FeSi$,^{5,6} Fe_3Al ,^{7,8} Fe_3Si ,^{9,10} and some compounds.¹¹⁻¹³ Niculescu *et al.*¹⁴ give an extensive review of $Fe_{3-x}T_xSi$ alloys for various transition metals T. The electronic structure of the Heusler compounds can range from metallic to semimetallic or semiconducting. A number of cases of half-metallic ferromagnetic phases, where the system is metallic for one spin direction and semiconducting for the other,^{15,16} have been identified. Examples of these are $Co_{2-x}Fe_xMnSi$ ^{17,18} and $Co_2MnSi_{1-x}Ge_x$,¹⁹ and the existence of anti-ferromagnetic ordering in some instances has been discussed.^{20,21} It is often possible to substitute on a specific metal site in the lattice with other magnetic or non-magnetic atoms, thereby inducing continuous changes in physical characteristics.²²⁻²⁴ In view of their tunable magnetic and transport properties, these compounds have attracted wide attention as potential electronic materials suitable for various applications.²⁵ With all this in mind, it is hardly surprising that Heusler-type compounds have been the subject of numerous theoretical and experimental studies over the years.

Recently, the compound Fe_2VAl has attracted special attention because of the intriguing behavior of its electrical resistivity, specific heat, and photoelectric properties.²⁶ The resistivity shows semiconductorlike behavior with a negative temperature coefficient suggesting an energy gap of ~ 0.1 eV. The photoelectron spectrum on the other hand seems to show a Fermi edge which precludes the existence of an energy gap wider than a few hundredths of an eV. Finally, low-temperature specific heat measurements for $T \rightarrow 0$ yield a term γT with $\gamma \sim 14$ mJ/mol K², which results in an effective mass about 20 times as large as the bare electron band mass. This mass enhancement is thought to originate from spin fluctuations^{27,28} or from excitonic correlations.²⁹ It makes Fe_2VAl a possible candidate for a 3d heavy-fermion system. A similar resistivity behavior has been reported for $Fe_{3-x}V_xGa$ with x near 1.0,³⁰ while $Fe_{2.4}V_{0.6}Si$ shows an onset of the same behavior.³¹

Concerning relevant *theoretical* studies, there is a substantial body of literature devoted to work on a variety of ordered Heusler-type phases and related systems. Among systems of present interest we mention Fe_3Si ,^{32,33} Fe_3Ga ,³⁴ Fe_3Al ,³⁵⁻³⁷ and Fe_2VAl .²⁷⁻²⁹ Little has been done on the disordered phases; we are only aware of the study of $Fe_{3-x}V_xSi$ alloys in Ref. 38, which is based on a non-selfconsistent crystal potential.

In the present article we report extensive first principles electronic structure computations on $Fe_{3-x}V_xX$ over the entire composition range for three different metalloids X, namely, Si, Ga, and Al. We consider the parent systems Fe_3X for which $x = 0$, while setting $x = 1$ yields the corresponding compounds Fe_2VX . By choosing $X=Ga$ or $X=Al$ the effect of replacing Si by either trivalent Ga or Al has been studied, and by varying x the entire composition range of disordered alloys is covered.

It is well-known that Heusler-type compounds display remarkable ‘site-selectivity’ properties^{39,40} in the sense that substituted metal atoms show a preference for entering the lattice in specific crystallographic positions. In the generic compound $Y_{3-x}Z_xX$, the metal atom Z generally prefers B sites in the lattice if Z lies to the left of Y in the periodic table, and the A or C positions if Z lies to the right of Y. We have carried out total energy

calculations which confirm this trend in $\text{Fe}_{3-x}\text{V}_x\text{Si}$.

An issue of interest concerns the validity of the so-called ‘local environmental’ model (reviewed in Ref. 14) which holds that the Fe moment scales with the number of Fe atoms in the nearest neighbor (nn) shell. The dilution of Fe(B) with non-magnetic V atoms in Fe_3Si will then yield a linear decrease in the Fe(A,C) moment, while the Fe(B) moment remains unchanged. The reason is that V substitution does not change the nn-shell of Fe(B) which continues to contain 8 Fe(A,C) atoms, while the number of Fe atoms in the nn-shell of Fe(A,C) decreases progressively. Our computations show substantial deviations from this simple picture in $\text{Fe}_{3-x}\text{V}_x\text{X}$, and imply that interactions beyond the nn-shell play a significant role in the behavior of electronic structure and magnetic moments. The computed spectra also yield insight into a number of other issues, such as the applicability of a rigid-band type picture in describing the effects of substitutions in Fe_3Si ,³² and the extent to which the ferromagnetism in $\text{Fe}_{3-x}\text{V}_x\text{X}$ ⁴¹ can be modeled as a rigid splitting of the paramagnetic bands. Finally, we clarify the nature of carriers in $\text{Fe}_{3-x}\text{V}_x\text{X}$ as a function of composition with consequences for transport phenomena^{30,31,42} in these materials.

We have attempted to make contact with relevant experiments as far as possible. Although our primary interest is in the composition dependence of various physical quantities, some intercomparisons for the end compounds Fe_3X and Fe_2VX are undertaken. The specific experimental data considered are: (i) the composition dependence of the total magnetic moment in $\text{Fe}_{3-x}\text{V}_x\text{X}$ for the three different metalloids, (ii) the site specific magnetic moments in the end compounds Fe_3X and Fe_2VX , and (iii) the soft x-ray emission spectra of Jia *et al.*⁴³ on Fe_3Si . Our theoretical predictions concerning the detailed variation of magnetic moments on the Fe(B), Fe(A,C), V, and Si sites in $\text{Fe}_{3-x}\text{V}_x\text{X}$ show interesting trends which should prove worthwhile to investigate experimentally.

Finally, a few words about our theoretical methods are in order. The disorder is treated within the framework of the charge- and spin-selfconsistent KKR-CPA methodology which we have developed and implemented in order to handle multi-component random alloys in a highly robust manner.^{18,44–50} We use the generalized tetrahedron method⁵¹ to carry out \mathbf{k} space integrations in disordered muffin-tin alloys, and as a result, our KKR-CPA codes allow us to treat the end compounds (Fe_3X and Fe_2VX) as well as the properties of single impurities in these limiting cases within a consistent, unified theoretical framework. We have also generalized the Lloyd formula⁴⁴ for the total number of states below any energy to multi-component alloys in an analytically satisfactory manner, permitting us an accurate evaluation of the Fermi energy in all cases. We are thus able to delineate clearly for the first time how the majority and minority spin states and magnetic moments in Fe_3Si develop when the Fe(B) position in the lattice is substituted by V atoms, and/or when Si is replaced by a metalloid of different valence. The results presented here are highly accurate and involve no parameters other than the experimental lattice constants, and constitute a reliable basis for testing the underlying KKR-CPA and local spin density (LSD) approximations.

An outline of this article is as follows. The introductory remarks are followed in Section II by an overview of our KKR-CPA formalism for multi-component alloys. The specific formulae used in computing various physical quantities discussed in this article are stated. Section III outlines the relevant structural aspects of the $\text{Fe}_{3-x}\text{V}_x\text{X}$ compounds. Section IV summarizes some technical details involved in our computations. Section V takes up the discussion and presentation of the results, and is divided into a number of subsections in

view of the quantity and complexity of the material involved. An effort has been made to keep the presentation as brief as possible.

II. AN OVERVIEW OF THE SPIN-DEPENDENT KKR-CPA FORMALISM FOR MULTI-COMPONENT COMPLEX ALLOYS

We consider a multi-component complex alloy where the Bravais lattice is defined by lattice vectors \mathbf{R}_n $\{n = 1, \dots, N\}$ with basis atoms in positions \mathbf{a}_k $\{k = 1, \dots, K\}$. K -sublattices can be generated from the basis points \mathbf{a}_k via lattice translations \mathbf{R}_n . For simplicity, we assume that one of these sublattices, k_{CP} , is occupied randomly by two types of atoms, A and B, with concentrations c_A and c_B , respectively. Other sublattices are taken to be perfectly ordered.⁵² The KKR-CPA formalism of interest here proceeds within the framework of an effective one electron Hamiltonian^{18,46–50,53,54} where the crystal potential is assumed to possess the form of non-overlapping muffin-tin spheres of radius S_k , i.e., the potential is spherically symmetric around each atom and constant (usually defined as the potential zero) in the interstitial region. Although such a Hamiltonian is more appropriate for a close packed metallic system, a reasonable representation of the crystal potential can often be obtained even in open crystals by adding suitably placed ‘empty’ spheres as basis ‘atoms’ in the lattice. Central for our purpose are matrix elements of the KKR-CPA ensemble-averaged Green function $G(E)$, and the one-site restricted Green function $G^{A(B)}$ where a specific atom $X_{k_{CP}}$ (A or B) sits on the central site of the disordered k_{CP} -th sublattice, while all other sites of the k_{CP} -th sublattice are occupied by the effective CPA atom. The relevant expressions are^{47,50,55–57}

$$\begin{aligned} \langle s', \mathbf{r}' + \mathbf{a}_{k_{CP}} | G^{A(B)}(E) | s, \mathbf{r} + \mathbf{a}_{k_{CP}} \rangle = & - \sum_{\sigma L} J_{\sigma L}^{A(B)}(s' \mathbf{r}') Z_{\sigma L}^{A(B)}(s \mathbf{r}) + \\ & + \sum_{\sigma' L', \sigma L} Z_{\sigma' L'}^{A(B)}(s' \mathbf{r}') T_{k_{CP} \sigma' L', k_{CP} \sigma L}^{A(B)} Z_{\sigma L}^{A(B)}(s \mathbf{r}), \end{aligned} \quad (2.1a)$$

$$\begin{aligned} \langle s', \mathbf{r}' + \mathbf{a}_{k_{CP}} | G(E) | s, \mathbf{r} + \mathbf{a}_{k_{CP}} \rangle = & c_A \langle s', \mathbf{r}' + \mathbf{a}_{k_{CP}} | G^A(E) | s, \mathbf{r} + \mathbf{a}_{k_{CP}} \rangle + \\ & c_B \langle s', \mathbf{r}' + \mathbf{a}_{k_{CP}} | G^B(E) | s, \mathbf{r} + \mathbf{a}_{k_{CP}} \rangle, \end{aligned} \quad (2.1b)$$

and

$$\begin{aligned} \langle s', \mathbf{r}' + \mathbf{a}_{k'} | G(E) | s, \mathbf{r} + \mathbf{a}_k \rangle = & - \sum_{\sigma L} J_{\sigma L}^{(k)}(s' \mathbf{r}') Z_{\sigma L}^{(k)}(s \mathbf{r}) \delta_{kk'} + \\ & \sum_{\sigma' L', \sigma L} Z_{\sigma' L'}^{(k')}(s' \mathbf{r}') T_{k' \sigma' L', k \sigma L}^{CP} Z_{\sigma L}^{(k)}(s \mathbf{r}), \text{ if } k \text{ and } k' \neq k_{CP}. \end{aligned} \quad (2.1c)$$

Here, $r' > r$, if $r > r'$ then J and Z should be transposed. $Z_{\sigma L}^{(k)}$ and $J_{\sigma L}^{(k)}$ are the regular and irregular solutions, respectively, of the radial Schrödinger equation within the k -th muffin-tin sphere, which may be written compactly as

$$\sum_{s=(+,-)} \{ (E + \nabla^2) \delta_{s's} - [v_0^{(k)}(\mathbf{r}) \delta_{s's} + v_1^{(k)}(\mathbf{r}) \hat{\mathbf{n}} \cdot \sigma_{s's}] \} Z_{\sigma L}^{(k)}(s \mathbf{r}) = 0, \quad (2.2)$$

where the up- and down-spin potentials at the k -th site, $v_+^{(k)}$ and $v_-^{(k)}$, are combined into a scalar part, $v_0^{(k)} = (v_+^{(k)} + v_-^{(k)})/2$, and a spin-dependent part, $v_1^{(k)} = (v_+^{(k)} - v_-^{(k)})/2$. $\hat{\mathbf{n}}$ is a unit vector along the direction of the magnetic moment. $\sigma = (\sigma_x, \sigma_y, \sigma_z)$ is a vector composed of Pauli matrices. $Z^{(k)}$ and $J^{(k)}$ are normalized such that outside the muffin-sphere (i.e., for $r > S_k$) they possess the form

$$Z_{\sigma L}^{(k)}(\mathbf{sr}) = \sum_{\sigma' L'} \chi_{\sigma'}(s) j_{l'}(\sqrt{E}r) Y_{L'}(\hat{\mathbf{r}}) [\tau_{\sigma' L', \sigma L}^{(k)}]^{-1} - i\sqrt{E} \chi_{\sigma}(s) h_l^+(\sqrt{E}r) Y_L(\hat{\mathbf{r}}), \quad (2.3a)$$

$$J_{\sigma L}^{(k)}(s\vec{\mathbf{r}}) = \chi_{\sigma}(s) j_l(\sqrt{E}r) Y_L(\hat{\mathbf{r}}). \quad (2.3b)$$

Here $Y_L(\hat{\mathbf{r}})$ is a real spherical harmonic, and $L = (l, m)$ is a composite angular and magnetic quantum number index. The spin index $\sigma = (+, -)$ and the spin variable $s = (+, -)$ allow the treatment of lattices with magnetic ordering. $\chi_{\sigma}(s) = \delta_{\sigma s}$ denotes the spin part of the wavefunction. $h^+(x) = j_l(x) + in_l(x)$ is a spherical Hankel function, where $j_l(x)$ is a spherical Bessel, and $n_l(x)$ a spherical Neumann function. The matrix $\tau^{(k)}(E)$ is built from on-the-energy-shell elements of the t-matrix of the atom X_k on the k -th site (or A, or B atom if $k = k_{CP}$). The elements of $\tau^{(k)}(E)$ are related to the corresponding phase shifts $\eta_{\sigma l}^{(k)}(E)$ by

$$\tau_{\sigma' L', \sigma L}^{(k)}(E) = -\sqrt{E} \exp(i\eta_{\sigma l}^{(k)}) \sin(\eta_{\sigma l}^{(k)}) \delta_{\sigma' \sigma} \delta_{L' L}. \quad (2.4)$$

The matrix T^A (or T^B) in Eq. (2.1) denotes the so-called central path operator (in the sublattice-site representation) for an A or B impurity placed in the KKR-CPA effective medium and is related to the medium path operator T^{CP} through the equation

$$T^{A(B)} = T^{CP} [1 + (\tau_{A(B)}^{-1} - \tau_{CP}^{-1}) T^{CP}]^{-1}. \quad (2.5)$$

In Eq. (2.5), matrix τ_{CP} is constructed from atomic matrices τ^{X_k} on sublattices with $k \neq k_{CP}$, and from the effective scattering matrix τ^{CP} on the k_{CP} -sublattice, i.e.,

$$[\tau_{CP}]_{k' \sigma' L', k \sigma L} = \begin{cases} \delta_{k' k} [\tau^{X_k}]_{\sigma' L', \sigma L}, & (k \neq k_{CP}), \\ \delta_{k' k} [\tau^{CP}]_{\sigma' L', \sigma L}, & (k = k_{CP}). \end{cases} \quad (2.6)$$

Similarly, for $\tau_{A(B)}$ we have

$$[\tau_{A(B)}]_{k' \sigma' L', k \sigma L} = \begin{cases} \delta_{k' k} [\tau^{X_k}]_{\sigma' L', \sigma L}, & (k \neq k_{CP}), \\ \delta_{k' k} [\tau^{A(B)}]_{\sigma' L', \sigma L}, & (k = k_{CP}). \end{cases} \quad (2.7)$$

The matrix T^{CP} in Eq. (2.5) is given by the Brillouin zone summation

$$T_{k' \sigma' L', k \sigma L}^{CP} = \frac{1}{N} \sum_{\mathbf{k} \in BZ} [\tau_{CP}^{-1} - B(E, \mathbf{k})]_{k' \sigma' L', k \sigma L}^{-1}, \quad (2.8)$$

with

$$[B(E, \mathbf{k})]_{k' L', k L} = \sum_{\mathbf{R}_{n' n}} \exp(i\mathbf{k} \mathbf{R}_{n' n}) [B(E)]_{k' L', k L}^{(n', n)}, \quad (2.9)$$

which are the KKR-complex crystal structure functions,⁵⁸ defined via a multipole expansion of the free electron Green function $G_0(E)$:

$$\begin{aligned} & \langle \mathbf{r}' + \mathbf{a}_{k'} + \mathbf{R}_{n'} | G_0(E) | \mathbf{r} + \mathbf{a}_k + \mathbf{R}_n \rangle = \\ & -i\sqrt{E} \sum_L j_L(\sqrt{E}r_<) h_l^+(\sqrt{E}r_>) Y_L(\hat{\mathbf{r}}') Y_L(\hat{\mathbf{r}}) \delta_{k'k} \delta_{n'n} + \sum_{L'L} Y_{L'}(\hat{\mathbf{r}}') [B(E)]_{k'L',kL}^{(n',n)} Y_L(\hat{\mathbf{r}}). \end{aligned} \quad (2.10)$$

The CPA-scattering matrix τ_{CP} in the Eq. (2.5) must be obtained by solving the KKR-CPA self-consistency condition

$$c_A T^A + c_B T^B = T^{CP}. \quad (2.11)$$

To solve Eq. (2.11) we use the iteration scheme based on the following expansion

$$\begin{aligned} [(T_n^{CP})^{-1} + (\tau_{CP}^{n+1})^{-1} - (\tau_{CP}^n)^{-1}]^{-1} &= c_A [(T_n^{CP})^{-1} + (\tau_A)^{-1} - (\tau_{CP}^n)^{-1}]^{-1} + \\ & c_B [(T_n^{CP})^{-1} + (\tau_B)^{-1} - (\tau_{CP}^n)^{-1}]^{-1}. \end{aligned} \quad (2.12)$$

Equation (2.12) allows the computation of $\tau_{CP}^{(n+1)}$ in terms of $\tau_{CP}^{(n)}$ and T_n^{CP} . By carrying out the integration of Eq. (2.8), T_{n+1}^{CP} is then determined, and the next iteration cycle can be started. This procedure is rigorously convergent and preserves the analytic properties of the solutions in the complex energy plane.^{59–62} This is crucially important because many other schemes used in the literature usually fail at some energy points. The problem generally becomes more severe as one considers systems with larger number of atoms per unit cell, and we have found that Eq. (2.12) must be the basis of any robust automated procedure for obtaining selfconsistent KKR-CPA solutions.

We have now completely defined the computation of the Green function in Eqs. (2.1) for a given crystal potential. For carrying out charge- and spin-selfconsistency cycles, one other key parameter, namely, the Fermi energy E_F , must be evaluated. In this connection, we have developed a powerful version of the Lloyd formula^{18,44,54,63} for the total number of states below any energy by formally integrating the trace of the KKR-CPA Green function exactly in the complex energy plane. The generalization of this formula to spin-dependent multi-atom alloys is given below. We emphasize that highly accurate charge- and spin-selfconsistent KKR-CPA results of the sort presented in this article would not be possible to obtain without the use of this Lloyd-type formula for determining the alloy Fermi energy. This is an important point because errors in the Fermi energy determination at any stage of the computation impede the convergence of selfconsistency cycles, and degrade the accuracy of the final solution for charge- and spin-densities as well as other physical properties.

We start by taking the trace of the KKR-CPA Green function over the spin- and position space, i.e.,

$$G(E) = \sum_{s=(+,-)} \sum_{k=1}^K \int_{V_k} d^3r \langle s, \mathbf{r} + \mathbf{a}_k | G(E) | s, \mathbf{r} + \mathbf{a}_k \rangle. \quad (2.13)$$

The integral in Eq. (2.13) extends over the Voronoi polyhedron V_k around the k -th site, and not the muffin-tin sphere, so that space is filled up exactly. Assuming a collinear magnetic structure (same z-axis on each site), the arguments of Ref. 44 can be extended straightforwardly to prove that

$$\begin{aligned}
G(E) = & TrQ + \frac{d}{dE} \left\{ \frac{1}{N} \sum_{\mathbf{k} \in BZ} Tr \ln[\tau_{CP}^{-1} - B(E, \mathbf{k})] \right\} - \\
& - \frac{d}{dE} \left\{ \sum_{k \neq k_{CP}} Tr \ln(\phi^{X_k}) + c_A Tr \ln(\phi^A) + c_B Tr \ln(\phi^B) \right\} \\
& + \frac{d}{dE} \{ Tr \ln[\tau_A^{-1} - \tau_B^{-1}] - c_B Tr \ln[\tau_{CP}^{-1} - \tau_A^{-1}] - c_A Tr \ln[\tau_{CP}^{-1} - \tau_B^{-1}] \},
\end{aligned} \tag{2.14}$$

where $\phi_{\sigma l}^{(k)}(E)$ is an energy-dependent renormalization factor for wavefunction $Z_{\sigma l}^{(k)}(E, r)$ defined by

$$Z_{\sigma l}^{(k)}(E, r) = \phi_{\sigma l}^{(k)}(E) \Psi_{\sigma l}^{(k)}(E, r) \tag{2.15}$$

with $\Psi_l^{(k)} \rightarrow r^l$ (for $r \rightarrow 0$). In Eq. (2.14), TrQ is the free electron contribution,

$$TrQ = \sum_{\sigma L} \sum_k \int_{V_k} d^3r j_l(\sqrt{E}r) Y_L(\hat{\mathbf{r}}) [-i\sqrt{E} h_l^+(\sqrt{E}r) Y_L(\hat{\mathbf{r}})] + \frac{d}{dE} \ln(\sqrt{E})^l. \tag{2.16}$$

Equation (2.14) is cumbersome to use in practical applications as it involves the on-shell elements of the t -matrices, τ , which do not extend properly into the complex energy plane; a form in terms of the logarithmic derivatives turns out to be more useful. First, we write the logarithmic derivative at the k -th muffin-tin sphere as

$$D_{k\sigma l}(E) = S_k^2 \frac{\partial}{\partial r} \ln Z_{\sigma l}^{(k)}(E, r)|_{r=S_k}. \tag{2.17}$$

The diagonal elements of the τ -matrices are related to the D -matrices by

$$\tau_{k\sigma l}^{-1}(E) = \frac{1}{j_l(\sqrt{E}S_k)} \frac{1}{D_{k\sigma l}(E) - D_{kl}^{(j)}} \frac{1}{j_l(\sqrt{E}S_k)} + i\sqrt{E} \frac{h_l^+(\sqrt{E}S_k)}{j_l(\sqrt{E}S_k)}, \tag{2.18}$$

where

$$D_{kl}^{(j)}(E) = S_k^2 \frac{\partial}{\partial r} \ln j_l(\sqrt{E}r)|_{r=S_k}. \tag{2.19}$$

We also require the angular-momentum representation of the free-electron Green function with position vectors on muffin-tin spheres,

$$\begin{aligned}
[G_0(E, \mathbf{k})]_{k'\sigma' L', k\sigma L} = & [D^{(h)} - D^{(j)}]^{-1} \delta_{\sigma'\sigma} \delta_{k'k} \delta_{L'L} + \\
& j_{l'}(\sqrt{E}S_{k'}) [B(E, \mathbf{k})]_{k'L', kL} j_l(\sqrt{E}S_k) \delta_{\sigma'\sigma}
\end{aligned} \tag{2.20}$$

where

$$D_{kl}^{(h)}(E) = S_k^2 \frac{\partial}{\partial r} \ln h_l^+(\sqrt{E}r)|_{r=S_k}. \tag{2.21}$$

Eliminating τ and B in favor of D and G yields our final formula

$$\begin{aligned}
G(E) = & -\frac{d}{dE} \left\{ \frac{1}{N} \sum_{\mathbf{k} \in BZ} Tr \ln[G_0^{-1}(E, \mathbf{k}) + D^{(j)} - D_{CP}]^{-1} \right\} \\
& - \frac{d}{dE} \{ c_A Tr \ln[\Psi_A^{-1} G^A] + c_B Tr \ln[\Psi_B^{-1} G^B] - Tr \ln G^{CP} \} \\
& + \frac{d}{dE} \left\{ \sum_{k \neq k_{CP}} Tr \ln[\Psi^{(k)}] \right\},
\end{aligned} \tag{2.22}$$

where

$$G^{A(B)} = [(G^{CP})^{-1} + D_{CP} - D_{A(B)}]. \quad (2.23)$$

Equation (2.22) is formally exact and possesses the form of a perfect derivative. Although several terms in Eq. (2.22) are real on the real axis, their inclusion is crucially important for obtaining an analytically correct form which can be used throughout the complex plane. Equation (2.22) not only accounts properly for all physical states, but also removes contributions from spurious singularities present in the scattering matrices and path operators. The formal integration of Eq. (2.22),

$$N(E) = -\frac{1}{\pi} \text{Im} \int_{-\infty}^E dE G(E), \quad (2.24)$$

immediately gives the total number of states, including all core states, below E_F . The value of E_F itself corresponds to the condition $N(E_F) = Z$, where Z is the total number of electrons in the Wigner-Seitz cell.

For a collinear magnetic structure, each spin direction can be treated separately via formula (2.13) yielding the spin-resolved DOS function

$$\rho_\sigma(E) = \frac{\partial}{\partial E} N_\sigma(E). \quad (2.25)$$

The magnetic moment μ of a W-S cell can be calculated from

$$\mu = N_+(E_F) - N_-(E_F). \quad (2.26)$$

The spin-dependent charge density at the k -th site is

$$\rho_\sigma^{(k)}(\mathbf{r}) = -\frac{1}{\pi} \int_{-\infty}^{E_F} dE \langle \sigma, \mathbf{r} + \mathbf{a}_k | G(E) | \sigma, \mathbf{r} + \mathbf{a}_k \rangle, \quad (2.27)$$

where, if $k = k_{CP}$, then the k -th atom is taken as an A or B atom and the site-restricted Green function of Eq. (2.1a) is used. The spin density at the k -th site is

$$s^{(k)}(\mathbf{r}) = \rho_+^{(k)}(\mathbf{r}) - \rho_-^{(k)}(\mathbf{r}). \quad (2.28)$$

The preceding equations allow the computation of KKR-CPA charge and spin densities in the alloy for a starting crystal potential. A new crystal potential may then be constructed via the use of the LSD exchange-correlation scheme. The iteration of this procedure leads to the fully charge- and spin-selfconsistent KKR-CPA electronic spectrum.

The magnetic moment on the k -th site,

$$\mu^{(k)} = \mu_B \int_{\Omega_k} d^3r s^{(k)}(\mathbf{r}), \quad (2.29)$$

is defined as an integral over the muffin-tin sphere volume Ω_k . Note that within the framework of the muffin-tin Hamiltonian, this is a unique way of defining site-dependent moments in a multi-component system. Since the muffin-tin spheres are not space filling, the sum of such individual moments will in general not equal the total moment in the unit cell obtained from Eq. (2.26) above, although the differences in the present case turn out to be rather small.

III. STRUCTURAL ASPECTS

A brief discussion of the salient features of the crystal structure will help the consideration of the electronic properties in the following section. The unit cell shown in Fig. 1 is a cube of side a and may be viewed as consisting of four interpenetrating fcc lattices denoted by the letters A through D; each atom in fact sits at the center of a cube of side $a/2$ with corners occupied by various atoms, so that the packing is identical to that of a simple bcc lattice. Fe_2VX possesses the classic L2_1 structure associated usually with the Heusler compounds. Here, the two Fe atoms occupy equivalent crystallographic positions A and C, while V sits on B sites, and the metalloid X on the D sites. The V atoms on the B sites are surrounded by 8 Fe nearest neighbors (nn's) in a bcc arrangement. Each of the Fe atoms in A or C positions has 4 V nn's (B) and 4 X nn's (D). The 4 metalloids (D) are located in a relative tetrahedral arrangement with respect to each other; this is also the case for the 4 V atoms in the B positions. These remarks make it clear that the Heusler compounds contain structural units characteristic of metals as well as semiconductors.

The substitution of V by Fe in Fe_2VX giving the disordered alloys $\text{Fe}_{3-x}\text{V}_x\text{X}$ causes no change in the nearest neighbor environment of the V atoms which continue to have 8 Fe nn's. The substituted Fe atoms in the B positions, on the other hand, possess 8 Fe nn's as in bcc Fe, in sharp contrast to the 4 Fe nn's around each Fe atom in Fe_2VX ; the end compound Fe_3X is thus rather close to bcc Fe. Although Fe_3X with two chemical species is classified as a DO_3 structure, note that in a solid state sense Fe_3X really contains three different types of 'atoms', i.e., two different Fe 'atoms' and the metalloid. It should furthermore be noted that, although the alloy $\text{Fe}_{3-x}\text{V}_x\text{Ga}$ crystallizes in the L2_1 structure, the end compound Fe_3Ga has the DO_3 structure only in the narrow temperature range $900\text{ K} < T < 920\text{ K}$. Below 900 K the stable phase for small x is the Cu_3Au -type (L1_2) structure. The DO_3 structure of Fe_3Ga is metastable and can be obtained by quenching.^{64,65}

The fact that V replaces the Fe atoms only in the B sites of Fe_3X has been adduced from NMR, Mössbauer and neutron diffraction measurements (see, e.g., Ref. 14). More generally, in the series $\text{Fe}_{3-x}\text{T}_x\text{Si}$ and $\text{Fe}_{3-x}\text{T}_x\text{Ga}$, where T denotes a transition metal, impurities to the left of Fe in the Periodic Table (Mn, V) show a strong preference for the B sites while those to the right (Co, Ni) enter at A or C sites. Interestingly, Cr seems to distribute almost randomly at A, B, and C sites in $\text{Fe}_{3-x}\text{Cr}_x\text{Si}$.⁶⁶ Reference 34 has considered the question of preferential occupation of various sites in the Fe_3Ga matrix via band-theory based total energy computations.

IV. COMPUTATIONAL DETAILS

We have carried out fully charge and spin self-consistent KKR-CPA computations on the series $\text{Fe}_{3-x}\text{V}_x\text{X}$, for $x = 0.0, 0.1, 0.25, 0.5, 0.75$ and 1.0 with the metalloid X being Si, Ga, or Al. In the case of the end compounds Fe_3X and Fe_2VX the KKR-CPA results were verified by extensive computations based on our totally independent KKR band-structure codes. The self-consistency cycles were repeated for each alloy composition until the *maximum* difference between the input and output muffin-tin potentials was less than 1 mRy at any mesh point in the unit cell. Therefore the final potentials used in the evaluation of various physical quantities are highly self-consistent. All calculations employ

a maximum angular momentum cut-off $l_{max}=2$ and the exchange-correlation functional of the Barth-Hedin form.⁶⁷

The four basis atoms were placed as follows: Fe(A)=(1/4,1/4,1/4), Fe(C)=(3/4,3/4,3/4), Fe(B) or V(B)=(1/2,1/2,1/2), and X(D)=(0,0,0). The experimental values of the lattice constants^{42,68,69} of Fe_3X are given in Table I. The lattice constant decreases by less than 1% in going from Fe_3Al to Fe_2VAl .⁷⁰ In contrast, the lattice constant slightly increases (less than 0.5%) with increasing V content in $\text{Fe}_{3-x}\text{V}_x\text{Si}$. In $\text{Fe}_{3-x}\text{V}_x\text{Ga}$ also the value of a differs by only about 1% between Fe_3Ga and Fe_2VGa .⁷¹ Thus, the composition dependence of the lattice constant in $\text{Fe}_{3-x}\text{V}_x\text{X}$ is rather weak, and in this work we have neglected the effect of this variation, and taken the a value for all compositions to be the same as that of the end compound Fe_3X .

The KKR-CPA cycles were carried out in the complex energy plane using an elliptic contour beginning at the bottom of the valence bands, and ending at the Fermi energy determined precisely to an accuracy of better than 0.1 mRy via the generalized Lloyd formula of Eq. (2.22). This elliptic contour was divided into 12 sections with 4 Gaussian quadrature points each, and thus contained a total of 48 energy points; the maximum imaginary part of the energy was 0.25 Ry. The KKR-CPA Green function in Eqs. (2.1) was computed on a 75 special \mathbf{k} point mesh⁷² in the irreducible part of the Brillouin zone (BZ) for each of the 48 aforementioned energy points in order to evaluate the BZ integral of Eq. (2.8). In this way the KKR-CPA self-consistency condition was solved at each of the 48 basic energy points to an accuracy of about 1 part in 10^5 , followed by the computation of a new spin-dependent crystal potential. The starting potential for the next cycle was typically obtained by a roughly 10% mixing of the new potential. The solution of the KKR-CPA condition required 1-10 iterations, while 10-50 charge and spin self-consistency cycles were usually needed depending upon the alloy composition to achieve convergence of the crystal potential to an absolute accuracy of about 1 mRy. For the final potentials, the total density of states (DOS), site-decomposed component densities of states (CDOS), and the l -decomposed partial densities of states (PDOS) were computed on a 201 energy point mesh in the alloys, and a 401 point mesh for the end compounds using a tetrahedral \mathbf{k} space integration technique⁵¹ (with division of 1/48-th of the BZ into 192 small tetrahedra) applicable to the ordered as well as the disordered muffin-tin systems.

V. RESULTS AND DISCUSSION

A. An Overview within a Simplified Model Density of States

We present first a relatively simple picture of the component densities of states associated with the transition metal atoms in $\text{Fe}_{3-x}\text{V}_x\text{X}$. The model density of states of Fig. 2 gives the majority (up) and minority (down) spin densities on Fe(A,C), Fe(B), and V sites in the limiting cases $x = 0$ and $x = 1$. The positions of the centers of gravity of the Si $3p$, Fe $3d$ and V $3d$ bands are shown, together with the Fermi energies (E_F) for the tetravalent (Si) and trivalent (Ga and Al) metalloids. In the following discussion we invoke Fig. 2 frequently in order to gain insight into the electronic structure and magnetism of $\text{Fe}_{3-x}\text{V}_x\text{X}$. We emphasize however that, even though the model of Fig. 2 captures a good deal of the physical essence of the underlying spectrum, the full KKR-CPA selfconsistent results should always be kept

in mind. This is especially true in the way Ga and Al-compounds are modeled in Fig. 2 via a rigid shift in the position of the E_F compared to the case of Si, the real situation of course being more complicated.

The relative positions of various levels in Fig. 2 can be used to obtain a qualitative handle on the movement of bonding and anti-bonding states on various atoms. This aspect will play an important role in our analysis below and, therefore, we comment briefly on this point with reference to Fig. 3 which describes the so-called common band model of bonding of d -band metals.⁷³ Consider two atoms, A and B, with atomic energy level $E_A^0 < E_B^0$, which are assumed to broaden into rectangular bands of common bandwidth W when the atoms are brought together to form a solid. From moment theory, it is known that the center of gravity of the local density of states (occupied and unoccupied) must coincide with the local on-site energy level $E_{A(B)}$ (which may be slightly shifted from the corresponding free-atom value in order to maintain local charge neutrality). The result is a skewing of the originally rectangular local density of states and a new bandwidth W_{AB} . Physically, the skewing represents a transfer of charge from the B atom to the A atom until the Fermi levels become the same. With this redistribution, the states at the bottom of the band (the bonding states) become more concentrated on the A atom while the antibonding states at the top of the band are found preferentially on the B atom as shown in Fig. 3b. This mechanism constitutes a basic ingredient for understanding the electronic structure and magnetism of $\text{Fe}_{3-x}\text{V}_x\text{X}$ considered below. A similar discussion based on the bonding of molecular orbitals has been given by Williams *et al.*³⁷

We are now in a position to consider the behavior of the total magnetic moment and its constituent parts in $\text{Fe}_{3-x}\text{V}_x\text{X}$ (Figs. 4-6) in terms of the simple model of Fig. 2. Some salient features which may be explained are as follows.

(i) *Smaller moment of Fe(A,C) compared to Fe(B) in Fe_3X .* Since the Fe(B) atom is surrounded by eight Fe(A,C) atoms in a bcc arrangement, it is not surprising to find the component density of states (CDOS) for the d electrons of Fe(B) in Fig. 2a to show the familiar structure of two peaks (bonding and anti-bonding) separated by a valley of low density of states found in bcc metallic Fe. For the up-spin electrons both peaks are occupied, while the exchange splitting pushes the down-spin antibonding peak above the Fermi level, resulting in a large magnetic moment on the Fe(B) site.

Concerning the Fe(A,C) moment, note first that Fe(A,C) is coordinated with four Fe(B) and four metalloids, and that the associated CDOS in Fig. 2 possesses extra states between the bonding and antibonding peaks. The main difference in relation to Fe(B) is in the behavior of the *down* spins for which Fig. 2a shows that $E_{\text{Fe(A,C)}} < E_{\text{Fe(B)}}$. Therefore, down-spin bonding states reside preferentially on Fe(A,C) and yield an increased negative spin density compared to Fe(B); the corresponding antibonding states on Fe(B) lie above E_F and are therefore unoccupied. Fe(A,C) and Fe(B) are quite similar with respect to the up spins since bonding as well as anti-bonding states on both Fe sites lie below the Fermi energy. The net result is that the total moment on Fe(A,C) is reduced compared to Fe(B).

(ii) *The negative moment of a V-impurity in Fe_3X .* We see from Fig. 2a that E_V is higher than $E_{\text{Fe(A,C)}}$ and its next-nearest neighbor $E_{\text{Fe(B)}}$ for the up-spin electrons, and thus the up-spin bonding states will move away from V sites; the antibonding states will be on V(B), but these lie mostly above the Fermi level and are thus unoccupied. On the other hand, for down spins E_V lies somewhat below $E_{\text{Fe(A,C)}}$ and $E_{\text{Fe(B)}}$. Both effects will tend to induce a

negative moment on V impurities.

(iii) *The negative moment of Si in Fe_3X .* The Si atoms too carry a negative moment, albeit small. The reason is that for the down-spin electrons E_{Si} lies well below $E_{Fe(B)}$, while for the up-spin electrons $E_{Si} > E_{Fe(B)}$. As a result of $p-d$ hybridization the down-spin bonding states will be more predominant on Si while the (empty) antibonding states will be found on Fe(B), resulting in a negative Si moment.

(iv) *Positive polarization of Fe(B) impurity in Fe_2VX .* Similar arguments explain why an Fe(B) impurity in Fe_2VSi , at the other end of the concentration range, is positively polarized. Figure 2b shows that $E_{Fe(B)} < E_{Fe(A,C)}$ for the up-spin electrons and thus the bonding states will be found predominantly on Fe(B). The opposite situation is true for the down-spin electrons. Both effects conspire to produce a strong positive Fe(B) moment.

(v) *Higher moment of Fe(A,C) but not Fe(B) in the Ga- and Al-compound compared to the Si-compound.* Going to $Fe_3Ga(Al)$ we find in Figs. 5 and 6 that, compared to Fe_3Si , the Fe(A,C) moments are higher. Figure 2a shows why. Ga and Al are trivalent and therefore the Fermi energy is lower. This does not affect the spin-up band which lies in its entirety below E_F , nor does it affect the Fe(B) spin-down band because there are hardly any states on Fe(B) in the region between the bonding and antibonding peaks. The net effect is a reduction of the number of spin-down electrons on Fe(A,C) with a resulting larger moment on Fe(A,C), and a negligible effect on the Fe(B) moment.

The preceding discussion is meant to be illustrative rather than exhaustive. Other features of the behavior of moments in Figs. 4-6 can be understood at least qualitatively along these lines.

B. Ordered compound Fe_3Si

After the introductory discussion of the electronic band structure of the $Fe_{3-x}V_xX$ system on the basis of the simple model introduced in the previous section we now turn to the calculated density-of-states curves in Fig. 7. A good understanding of Fe_3Si is essential for delineating the effects of substitution on the metalloid and/or the Fe(B) site considered in the following sections. Note that the Si 3s and 3p bands show little overlap (Figs. 7c4 and 7c3) in Fe_3Si , even though in Si the 3s and 3p bands possess a substantial overlap; this is the result of an increased Si-Si distance in Fe_3Si compared to Si.

The bonding between Si and Fe is complex and involves s and p electrons of Si and s, p as well as d electrons of Fe. Some manifestations of this bonding are as follows. The Si 3s states form a semicore band extending below ~ 0.2 Ry; the presence of a finite density of states on both Fe sites in this energy region indicates Si-Fe interaction involving Si 3s electrons, even though there are no Si atoms in the Fe(B) nn shell. Si-Fe binding via Si and Fe p electrons is apparent from the presence of the three-peak structure in the p bands, which is most clearly discernable in the Si down-spin p band (Fig. 7c3), but is also present in the up- and down-spin p bands of both types of Fe sites. Finally, there is the effect of hybrid formation between the 3p states of Si and the d states of Fe described by Ho *et al.*⁷⁴ and discussed in Ref. 37 in connection with Fe_3Si , which tends to concentrate $p-d$ bonding states on Fe(B) and enhance the moment on Fe(B).

The behavior of $N(E_F)$, the density of states at E_F , deserves comment. The states at E_F possess mostly d character with some p admixture (Fig. 7). The Fe(A,C) contribution

dominates, with the spin-down part being much larger than the spin-up part (Fig. 7a1). By contrast, the Fermi level on Fe(B) lies in a fairly low density of states region in the up- as well as the down-spin CDOS. The energy dependence of the CDOS in the vicinity of E_F is also quite different on various sites. On Fe(A,C), the Fermi level lies near a dip in the up-spin CDOS, but in a rapidly decreasing region in the down-spin CDOS (Fig. 7a1); a rigid upward shift of 0.04 Ry in E_F , for example, would cause a reversal of spin polarization at E_F . The situation for Fe(B), on the other hand, is quite the opposite in that a similar shift in E_F will induce a rapid increase in the down-spin density (Fig. 7b1).

Our computed ℓ -decomposed Si-CDOS (Fig. 7c) gives insight into the Si $L_{2,3}$ soft x-ray emission (SXE) spectrum of Fe_3Si reported by Jia *et al.*⁴³ The SXE data from Fe_3Si (see Fig. 1 of Jia *et al.*) display three distinct peaks centered at binding energies of 2 eV, 6 eV, and 10 eV. To interpret these results recall first that the $L_{2,3}$ SXE will only involve s and d but not the p partial density due to the $\Delta\ell = \pm 1$ selection rule for optical transitions. The d PDOS (Fig. 7c2) contains many features extending from 0-6 eV below E_F . In Fig. 8 we have plotted the sum of s and d PDOS for Si after smoothing the theoretical spectrum to reflect experimental broadening.⁷⁵ The three peaks in Fig. 8 at binding energies of 1.7 eV, 5.5 eV, and 9.2 eV, are seen to be remarkably consistent with the experimental values quoted above. In particular, our calculations suggest that the 6 eV peak in the SXE spectrum involves Fe-Si bonding d states since both Fe(B) and Fe(A,C) CDOS's possess a substantial density in this energy region (Figs. 7a1 and 7b1, note the scale); in contrast, Ref. 43 associates this peak with sp^3 bonded Si orbitals.⁷⁶

C. Ordered compounds Fe_3Ga and Fe_3Al

Fe_3Si and Fe_3Ga are compared first (Fig. 9). The replacement of Si by Ga is seen to induce only small changes in the shape of the down-spin CDOS on either Fe(A,C) or Fe(B), aside from a relative lowering of the Fermi level to account for the reduced valence of the metalloid. The effect on the up-spin CDOS, on the other hand, is more substantial in that the shape of both Fe(A,C) and Fe(B) is flatter around E_F in Fe_3Ga compared to Fe_3Si (e.g., Figs. 9a2 and 9b2); the Fe-Ga interaction pulls the up-spin states peaking around the Fermi level in Fe_3Si to lower energy.

The spectra for Fe_3Ga and Fe_3Al in Fig. 9 are quite similar. As already noted, the Si s band in Fe_3Si (below ~ 0.2 Ry) is more or less core-like; the Ga s band lies at a lower binding energy closer to the bottom of the valence band in Fe_3Ga . This progression continues in Fe_3Al where the Al s band overlaps the bottom of the valence band causing a relatively greater distortion of states in this energy region (see bottom row in Fig. 9).

It is noteworthy that substitution on the Si site by Ga and Al not only influences the Fe(A,C) but also the Fe(B) CDOS. This is consistent with our observation above in connection with Fig. 7 that the metalloid affects the Fe(B) CDOS even though there are no metalloid atoms in the Fe(B) nn-shell. It is clear, therefore, that a simple 'environmental' type model^{14,32} which is based on taking account of *only* the composition of the nn-shell possesses intrinsic limitations in describing the electronic structure and magnetism of Fe_3X .

D. Ordered compounds Fe_2VX ($\text{X}=\text{Si, Ga, Al}$)

The substitution of V for Fe(B) in Fe_3Si is seen by comparing Figs. 9a and 10a to dramatically alter the density of states. The substitution of the high-moment Fe atom by nonmagnetic V causes the magnetic moment to nearly collapse. This is reflected in somewhat different ways in the up- and down-spin densities. Similar to Fe(B), the V atom in a bcc environment displays the familiar d band structure of two peaks separated by a region of low density, but since V is nonmagnetic the exchange splitting is close to zero (Fig. 10a3). In order to accommodate the reduced valence of V compared to Fe, both the up- and down-spin antibonding V d states are pushed above E_F . The net changes in relation to Fe_3Si are most clearly visible for the up-spin electrons. The up- and down-spin densities of Fe_2VSi possess similar shapes with the small magnetic splitting localized essentially on Fe(A,C). The dip in the up-spin Fe_3Si DOS around 0.6 Ry in Fig. 9a1, now moved up on the energy scale, is partially filled by nnn Fe states around 0.75 Ry (Figs. 10a1 and 10a2). To the left of these there is a complex of Fe-V bonding states followed by metalloid $p-d$ bonding states (Figs. 10a2 and 10a3). Between the Fe states and the antibonding Fe-V states around the Fermi level a near gap has formed for both spin directions.

The character of states at the Fermi level differs greatly between Fe_2VSi and Fe_3Si ; the B site (i.e., V(B) *vs* Fe(B)) contribution is larger in the former compared to the latter. The DOS at E_F is much larger in Fe_2VSi and is dominated by Fe(A,C) and V(B) up spins, while in Fe_3Si the Fe(A,C) down spins dominate with other contributions being small. Other differences are evident from Figs. 9a and 10a; for example, E_F lies in up-spin Fe(A,C) and V(B) peaks in Fe_2VSi , but in an up-spin Fe(A,C) dip in Fe_3Si . Therefore, we should expect Fe_2VSi to respond very differently to rigid shifts of the Fermi energy.

Turning to Fe_2VGa (Fig. 10b), the spectra are quite similar in shape to Fe_2VSi , although the minimum in the DOS around 0.8 Ry is somewhat deeper and broader in the Si compound. That the spectrum of Fe_2VGa does not possess an actual band gap but only a pseudogap for either spin direction is seen more clearly from Fig. 11. The small downward shift of the Fermi level due to the lower valence of Ga places the Fermi level firmly in the (pseudo)gap region, thereby precluding moment formation. In sharp contrast to the Si compound, therefore, the DOS at E_F in the Ga case is nearly zero for up- as well as down-spins and would increase rapidly by a rigid lowering or raising of the Fermi level.

Notably, the gap between the semicore band around 0.15 Ry and the bottom of the valence band in Fe_2VSi is larger than in Fe_3Si . This effect is present also in Fe_2VGa , and is a consequence of changes in the various interactions and not due to a change in the lattice size since we have used a lattice constant independent of V concentration in our computations. The results for Fe_2VAl are seen to be similar to those for Fe_2VGa . However, in contrast to the case of Fe_3Al (Fig. 9c), the bottom of the valence band does not overlap the semicore band around 0.25 Ry in Fe_2VAl (Fig. 10c).

E. Disordered alloys $\text{Fe}_{3-x}\text{V}_x\text{X}$ ($\text{X}=\text{Si, Ga, Al}$)

1. $\text{Fe}_{3-x}\text{V}_x\text{Si}$

$\text{Fe}_{3-x}\text{V}_x\text{Si}$ is considered first with the help of Fig. 12. The basic effects outlined in the preceding subsection in connection with Fe_2VSi are of course at play here. Since the driving mechanism is the replacement of Fe(B) by V(B), the b and c panels in Fig. 12 will be considered first. At $x = 0$ (Fig. 12b1) the Fe(B) site displays the two-peaked structure discussed earlier. A V impurity on that site however shows already the upward shift of the two peaks in the up-spin d band. This shift, together with the interaction of the V atom with its Fe(A,C) neighbors, has been shown in Subsection V A above to lead to the negative moment on the V impurity.

As the V concentration increases, the Fe(B) density of states shows the familiar blurring caused by disorder scattering in the alloy. This effect is however highly non-uniform in that some states are broadened much more than other states, which reflects large variations in the effective disorder parameter as a function of \mathbf{k} , E , and spin polarization.⁷⁷ Also, with increasing x the down-spin bonding peak at 0.7 Ry decreases in size (Fig. 12b), leaving an even larger uncompensated moment in the up-spin band. In the dilute Fe impurity limit (Fig. 12b5) the moment on this Fe(B) atom is found to be $3.08 \mu_B$. It is interesting to see that in this limit the Fe(B) up-spin bands are virtually undamped again; they have the character of relatively sharp impurity levels.

As a result of the interaction with the V and Fe atoms on the B sites, the Fe(A,C) CDOS undergoes quite substantial changes. With increasing V content, the highest occupied peak around 0.8 Ry in the up-spin Fe(A,C) CDOS moves to higher energies, which helps deepen the low density of states region near the Fermi level and pushes E_F to higher values. These large movements in the spectral weights are not present in the down-spin Fe(A,C) CDOS although the development of the pseudogap takes place in this case also. The net result of the spectral weight shifts is a decrease of the up-spin moment and a simultaneous increase of the down-spin moment due to the upward shift of the Fermi level. The two effects conspire to cause a rapid depolarization of the Fe(A,C) sites. For $x \geq 0.5$ the aforementioned effects more or less saturate and there is little further change in the various moments.

The magnetic moments associated with different sites are seen from Fig. 4 to deviate from straight lines joining the $x = 0.0$ and $x = 1.0$ values. The moments change essentially linearly for $x \leq 0.5$ with the Fe(B) component increasing while the Fe(A,C) component and the absolute value of the negative moment on V(B) decrease. For larger V concentrations, all contributions are nearly flat. Essentially, as Figs. 12 and 2 show, there are three interfering mechanisms in going from Fe_3Si to Fe_2VSi : (i) Replacement of high-moment Fe(B) by low-(negative)-moment V(B) atoms; (ii) a gradual upward movement of the up-spin Fe(A,C) antibonding orbitals which reduces the Fe(A,C) moment, and (iii) in going from Fe_3Si to Fe_2VSi , as the number of Fe(B) atoms decreases, the Fe(A,C) atoms play an increasingly important role in bonding. The concentration dependence of the magnetic moments and their lack of linearity results from an interplay of these factors.

We have made an extensive comparison of our results on $\text{Fe}_{3-x}\text{V}_x\text{Si}$ with those of Kudrnovsky *et al.*³⁸ Despite some overall similarities, our results differ substantially from those of Ref. 38. For example, the Fermi level in our case lies at or near a dip in the *majority* spin-DOS for up to 50% V (Fig. 12a), while in Ref. 38 (see their Fig. 8), the majority spin $N_+(E_F)$ decreases with increasing energy in the 0% and 25% alloy and is essentially at a

minimum in the 50% V case. The Fermi level in Ref. 38 rises uniformly with increasing V content. In sharp contrast, our E_F changes non-linearly, with the E_F values being rather close for 0% and 25% V (Figs. 12a1 and 12a2). The site-dependent CDOS's show differences as well. The shape of the Fe(B) majority spin-CDOS is seen from Fig. 12b to change considerably in the energy region lying a few eV's below E_F . In Ref. 38 (see their Fig. 10), on the other hand, the Fe(B) majority-spin CDOS possesses a roughly composition independent three peaked shape. The Fe(B) CDOS at E_F in our computations is quite small for all V concentrations, while in Ref. 38 the minority-spin Fe(B) CDOS at E_F is quite large (see their Fig. 9). Turning to magnetic moments, we find (Fig.4) the Fe(B) moment to *increase* with V content, whereas Ref. 38 obtains a *decreasing* Fe(B) moment. Further, our moments on all sites vary linearly up to 50% V and remain virtually constant thereafter, and the total moment shows a related break in slope around 50% V. The results of Ref. 38 do not display these effects clearly as all moments appear to vary roughly linearly up to 75% V. The comparisons of this paragraph make it clear that the charge selfconsistency achieved in the present work has important consequences for the electronic spectrum; as already noted, the results of Ref. 38 are based on a non-selfconsistent crystal potential.

2. $Fe_{3-x}V_xGa$ and $Fe_{3-x}V_xAl$

The evolution of the electronic spectrum of $Fe_{3-x}V_xGa$ (Figs. 13) can be understood along much the same lines as $Fe_{3-x}V_xSi$, keeping in mind of course the differences in the spectra of the end compounds discussed already in Sections V B and V C above. Interestingly, there are differences between the composition dependence of the magnetic moments between the two compounds as seen by comparing Figs. 4 and 5. In $Fe_{3-x}V_xSi$, the computed moments on all sites remain essentially constant for $x \geq 0.5$, whereas in $Fe_{3-x}V_xGa$ the moments on Fe(A,C) and V(B) continue to decrease, and that on Fe(B) continues to increase with x . These effects can be related to the behavior of the underlying spectra as follows. Concerning Fe(A,C), note that changes in the Fe(A,C) CDOS for either spin direction are quite similar in the Ga and the Si compound insofar as the development of the pseudogap around the Fermi level and the shifts of spectral weights in the majority spin CDOS (Figs. 12a and 14a) are concerned. In $Fe_{3-x}V_xSi$, the Fermi level lies in the down-spin pseudogap for $x \geq 0.5$. But, the smaller valence of Ga (compared to Si) causes E_F in $Fe_{3-x}V_xGa$ to be relatively lower. The minority spin contribution to the Fe(A,C) moment then continues to increase for $x \geq 0.5$ in $Fe_{3-x}V_xGa$, with a concomitant decrease in the total Fe(A,C) moment.

The composition dependence of the electronic spectrum as well as the magnetic moments on various sites in $Fe_{3-x}V_xAl$ is quite similar to that of $Fe_{3-x}V_xGa$, minor differences notwithstanding. While the moments in $Fe_{3-x}V_xAl$ are presented in Fig. 6, the detailed results for Fe(A,C), Fe(B), and V(B) CDOS's are not shown in the interest of brevity.

F. Other aspects

1. Rigid band model vs common-band model

Although some features of the Ga and Al alloys can be understood reasonably via a rigid band picture (see discussion of Fig. 2 above), our results indicate that a description of the electronic spectrum of $\text{Fe}_{3-x}\text{V}_x\text{X}$ in terms of any simple rigid-band-type model is generally unjustified. The end compounds Fe_3X and Fe_2VX possess quite different spectra for any given metalloid X, and the shapes of the CDOS's at various sites change with Fe/V substitution. Furthermore, the fact that the up- and down-spin DOS's possess very different shapes, particularly in the Fe_3X limit, implies that the ferromagnetic state cannot be described properly to be the result of a simple spin splitting in the form of a Stoner shift of more or less rigid paramagnetic bands. However, from our discussion it is clear that the common-band model constitutes a fertile framework for obtaining insight in the electronic structure and magnetism of these materials. While the exchange splitting on the Fe(B) atom constitutes the driving force for magnetism in these compounds, the hybridization between different states and the resulting differences between the weights of various bonding and antibonding states on different atoms lead to a rich variety of behaviors.

2. Site selectivity

As pointed out in Section III, the issue of site selectivity in the Heusler-type alloys has been the subject of numerous studies,^{14,32–34,78} with the attention being focused mostly on determining whether other metal atoms when substituted for Fe preferentially occupy Fe(B) or Fe(A,C) sites in the lattice. The high electronegativity of Si implies that Si attracts electrons from the surrounding Fe atoms. Our calculations indicate that in Fe_3Si the number of electrons inside the muffin-tin spheres of Fe(A,C) is 25.115 against 24.975 for Fe(B), i.e., Fe(A,C) *averaged over both spin directions* is more electronegative than Fe(B). The same is true in Fe_3Ga and Fe_3Al , even though Ga and Al are less electronegative than both Fe(A,C) and Fe(B). The Coulomb energy of the crystal lattice will be reduced if electronegative Fe(A,C) is replaced by an element more electronegative than Fe (i.e., Co or Ni) or if Fe(B) is replaced by a less electronegative element (i.e., Ti, V, Cr, or Mn), thus explaining the observed site selectivity. A more quantitative demonstration of these effects, of course, must be based on total energy calculations where the LDA has proved a sound basis for metals,⁷⁹ compounds,^{37,80} and binary alloys.⁸¹ Accordingly, we have computed the total energy of the alloy $\text{Fe}_{3-x}\text{V}_x\text{Si}$ for a number of concentrations x putting V atoms first on the A or C sublattice and subsequently on the B sublattice. Figure 15 shows the difference between the total energy for each of these two situations and the sum of the energies of the constituent atoms for $x \leq 0.08$. It is clear that the total energy is lowered when the V atom occupies a B site.

3. Electrical resistivity

Figures 12-14 imply that the type, spin, and number of carriers available for transport in the $\text{Fe}_{3-x}\text{V}_x\text{X}$ alloys depend strongly on the V content as well as on the metalloid valence. Focusing on $\text{Fe}_{3-x}\text{V}_x\text{Si}$ first, we see from Fig. 12 that in Fe_3Si (topmost row) the density

of states at the Fermi level is dominated by the down-spin Fe(A,C)-CDOS. Therefore, the current in Fe_3Si will be carried primarily by down-spin electrons associated with Fe(A,C) sites with relatively little contribution from Fe(B) and V(B) sites. With increasing V content, the Fermi level in $\text{Fe}_{3-x}\text{V}_x\text{Si}$ moves into the pseudogap in the down-spin Fe(A,C)-CDOS; for $x=0.50$, these electrons are seen to be essentially frozen out of the transport processes. In fact, for $x=0.50$ few carriers of either spin are available and one expects the material to possess a high resistivity. For $x=0.75$, the up-spin Fe(A,C)-CDOS is larger, and the up-spin V-CDOS begins to increase. In the limiting case of Fe_2VSi (Fig. 12, bottom row), we see that the current will be carried mainly by up-spin Fe(A,C) and V(B) electrons. Thus, in going from Fe_3Si to Fe_2VSi , the carriers change from being dominated by down-spin Fe(A,C) electrons to up-spin Fe(A,C) and V(B) electrons, and the material goes through a high-resistivity range for intermediate compositions. Experiment confirms this picture: measurements of the residual resistivity as a function of x in $\text{Fe}_{3-x}\text{V}_x\text{Si}$ by Nishino *et al.*³¹ show a pronounced maximum at $x \sim 0.4$.

The situation with $\text{Fe}_{3-x}\text{V}_x\text{Ga}$ is seen from Fig. 14 to be similar to that of $\text{Fe}_{3-x}\text{V}_x\text{Si}$, except that the compound does not display an intermediate range with few carriers around $x=0.50$. Instead, the carriers continue to be dominated by down-spin Fe(A,C) electrons for all compositions, with the total number of available carriers going nearly to zero in the $x=1.0$ limit. There seems to be a curious effect in the $x = 0.75$ case (Fig. 14b4) in that the Fe(B) CDOS displays a substantial up-spin component, suggesting that this alloy may show unusual transport phenomena.

Returning to the compounds Fe_2VAl and Fe_2VGa , we note that the Fermi surface of Fe_2VGa is very similar to that of Fe_2VAl .^{27,28} It consists of three small hole pockets at Γ and an electron pocket at X (see Fig. 11), resulting in a very small number of carriers.⁸² Recent calculations for Fe_2VAl which include spin-orbit coupling²⁹ find a further reduction in carrier density. This would make these compounds semimetals or even semiconductors, although the latter would disagree with a Fermi cut-off reported by Nishino *et al.*²⁶ in Fe_2VAl using high-resolution photoemission. Another cause for the high and strongly temperature and composition dependent resistivity could be strong electron scattering by spin fluctuations. Although we find Fe_2VAl and Fe_2VGa to be virtually non-magnetic in the V-rich regime, we have seen that they may nevertheless contain sizable, relatively isolated, local moments in the form of Fe atoms on V(B) positions, accompanied by non-stoichiometry or frozen-in antisite defects. The band structure of these compounds consists of a set of rather flat Fe and V d bands closely below and above the Fermi level. A similar situation involving f bands is known to lead to heavy-fermion behavior in a variety of intermetallic compounds. Also, the temperature dependence of the resistivity in Fe_2VAl is qualitatively very similar to that of well-known heavy-fermion compounds such as CeCu_2Si_2 and CeCu_6 .⁸³ Thus, the resistivity behavior in Fe_2VAl and Fe_2VGa may be a signature of heavy-fermion behavior in a $3d$ intermetallic compound. It is also interesting to note that the concentration $x = 0.6$ at which $\text{Fe}_{3-x}\text{V}_x\text{Si}$ shows similar resistivity behavior³¹ lies in the concentration range where the Fermi level is at or very near the strong dip in the density of states which for $x \rightarrow 1.0$ develops into the pseudogap. This suggests that a low carrier density, possibly in combination with strong local moments, is a necessary ingredient for semiconductorlike resistivity behavior in these alloys and compounds. In this respect resistivity measurements in $\text{Fe}_{3-x}\text{V}_x\text{Si}$ for $x > 0.6$ would be of interest.

4. Magnetic moments—comparison with experiment

We comment now on the magnetic moment data given in Table II for the end compounds.^{10,27,28,33–35,37,38,42,84–86} The experimental data in this table is not meant to be exhaustive; we focused on sources which report site-dependent magnetic moment information. Fe₃Si has been investigated most extensively. The situation with the Fe(B) moment in Fe₃Si appears to be good in that the experimental values lie around 2.2-2.4 μ_B , and are in reasonable accord with the theoretical value of about 2.5 μ_B ; the value of 1.9 μ_B is based on a tight-binding model computation. A similar level of agreement is also seen generally on the Fe(B) site in Fe₃Ga and Fe₃Al. In the case of the Fe(A,C) moment, on the other hand, the situation is somewhat less satisfactory as the experimental as well as theoretical values are more scattered. Theoretically, the metalloid is predicted to exhibit a weak negative polarization, but no experimental results are available. Lack of experimental data is also evident for the magnetic moments in Fe₂VX; notably, experiments of Ref. 87 give a near zero Fe(A,C) moment in Fe₂VSi in disagreement with computed values of 0.43 μ_B (this work), and 0.37 μ_B by Ref. 38. Interestingly, Endo *et al.*²¹ report antiferromagnetic ordering in Fe₂VSi; on this basis, an Fe(A,C) moment of 0.5-1.0 μ_B has been deduced.⁸⁸ Of course, it should be remembered that our calculations do not include an antiferromagnetic ground state.

Also for the alloys Fe_{3-x}V_xX we are not aware of any experimental work addressing contributions of individual sites to the total moment. In Fe_{3-x}V_xSi (Fig. 4), the computed total moments are rather close to the measurements of Ref. 14, although further experimental work in the V-rich alloys, where the total moment curve is predicted theoretically to display a significant change in slope, would be interesting. The experimental data in the Ga⁶⁵ and Al⁸⁹ compounds (Figs. 5 and 6) extend over a wider composition range and here again there is a reasonable level of accord with the theory, even though the experimental points are generally lower, especially for the 50% V alloy. We should keep in mind however that our calculations assume a perfectly random occupation of Fe(B) sites by V atoms while the physical system may display short range ordering and clustering effects in addition to possible uncertainties associated with site occupancies.

VI. SUMMARY AND CONCLUSIONS

We have discussed the electronic structure of Fe_{3-x}V_xX Heusler alloys, where the metalloid X is Si, Ga, or Al, on the basis of our all-electron, charge- and spin-selfconsistent KKR-CPA computations. Specific compositions calculated include the concentrated alloys with 25, 50, and 75 atomic percent V substituted randomly in the Fe(B) site, the end compounds Fe₃X and Fe₂VX, and the limiting cases of a single V impurity in Fe₃X and a single Fe(B) impurity in Fe₂VX. All calculations were carried to a high degree of selfconsistency and are parameter-free excepting the use of experimental lattice constants. The Fermi energy was evaluated in all cases with a high degree of precision by using a generalized Lloyd formula for multi-component systems. The use of a tetrahedron-type **k** space integration method, which we have extended to handle disordered muffin-tin systems, allows us to treat the ordered end compounds as well as the single impurity limits on an equal footing with the concentrated alloys. Our results thus provide a reliable basis for testing the underlying

framework of the KKR-CPA and LSD approximations. To our knowledge, little theoretical work exists in the literature concerning the electronic structure of disordered phases of Heusler alloys, although Ref. 38 has previously considered aspects of $\text{Fe}_{3-x}\text{V}_x\text{Si}$ based on non-selfconsistent computations.

Highlights of our results are as follows. An examination of the spin-dependent component densities of states (CDOS's) at various sites in $\text{Fe}_{3-x}\text{V}_x\text{Si}$ shows that the replacement of Fe(B) by V induces substantial shifts in spectral weights, especially in the up-spin Fe(A,C) CDOS; the down-spin Fe(A,C) CDOS and the CDOS for either spin direction at other sites – Fe(B) or Si – suffer relatively lesser changes. A pseudogap develops around the Fermi energy in the up- as well as the down-spin density of states in the V-rich regime. The effects of V substitution in $\text{Fe}_{3-x}\text{V}_x\text{Ga}$ are similar to those in $\text{Fe}_{3-x}\text{V}_x\text{Si}$, although a number of differences arise from the reduced metalloid valence and the changes in the metal-metalloid interaction. $\text{Fe}_{3-x}\text{V}_x\text{Al}$, on the other hand, possesses a spectrum rather close to that of $\text{Fe}_{3-x}\text{V}_x\text{Ga}$, some differences in detail notwithstanding.

The complex spectral changes in the electronic spectra of $\text{Fe}_{3-x}\text{V}_x\text{X}$ induced by Fe(B)/V substitution and by the effects of metal-metalloid interaction cannot be described within a rigid band picture based on one of the end compounds. In a similar way, the ferromagnetism of these alloys cannot be viewed as a rigid splitting of the related paramagnetic spectra. However, the common band model in which the bonding between atoms is described by the formation of a common energy band containing bonding and antibonding states with different weights on the participating atoms provides insight into the electronic structure of these compounds.

We have analyzed the composition dependence of the magnetic moments associated with individual sites in $\text{Fe}_{3-x}\text{V}_x\text{X}$ in detail, and correlated these changes with those in the underlying spectra. In $\text{Fe}_{3-x}\text{V}_x\text{Si}$, all moments vary essentially linearly for $x \leq 0.50$, and remain virtually constant thereafter. V substitution (up to 50% V) decreases the Fe(A,C) moment, but *increases* the Fe(B) moment; Si possesses a very small ($-0.08 \mu_B$) negative moment. The V impurity in Fe_3Si possesses a negative moment of $-0.62 \mu_B$. The total moment in $\text{Fe}_{3-x}\text{V}_x\text{Si}$ varies non-linearly over $0 \leq x \leq 1.0$ with a change in slope at $x = 0.50$. This behavior differs sharply from that expected on the basis of the ‘local environment’ picture which assumes the Fe(A,C) moment to decrease linearly over $0 \leq x \leq 1.0$ and the Fe(B) moment to remain constant. On the other hand, the moments in $\text{Fe}_{3-x}\text{V}_x\text{Ga}$ and $\text{Fe}_{3-x}\text{V}_x\text{Al}$ show a different type of non-linearity in that the Fe(A,C) moment decreases rapidly between $0.5 \leq x \leq 0.75$, and the aforementioned ‘saturation’ effect in $\text{Fe}_{3-x}\text{V}_x\text{Si}$ for $x > 0.50$ is not seen. These results show clearly that the metal-metalloid interaction has an important bearing on the magnetism of Heusler alloys. Some measurements of the total magnetic moment in $\text{Fe}_{3-x}\text{V}_x\text{Si}$, $\text{Fe}_{3-x}\text{V}_x\text{Ga}$, and $\text{Fe}_{3-x}\text{V}_x\text{Al}$ are available, and in this regard our theoretical results are in reasonable agreement with the experimental values. Further experimental work particularly to obtain site decomposed moments in $\text{Fe}_{3-x}\text{V}_x\text{X}$ should prove worthwhile. Finally, we have delineated the nature of carriers involved in transport processes in $\text{Fe}_{3-x}\text{V}_x\text{X}$. In the $x = 0$ limit, most of the carriers originate in the down-spin Fe(A,C) sites. With increasing V concentration, as a pseudogap forms around the Fermi energy, the total number of carriers in $\text{Fe}_{3-x}\text{V}_x\text{Si}$ decreases rapidly. In the V-rich alloy, the number of carriers begins to increase once again, but it is now dominated by up-spin electrons. By contrast, the V-rich compounds in the case of $\text{Fe}_{3-x}\text{V}_x\text{Ga}$ or $\text{Fe}_{3-x}\text{V}_x\text{Al}$ are

predicted to be semimetallic, and to be dominated by down-spin carriers throughout the composition range. These dramatic changes in the number, spin, and type of carriers in $\text{Fe}_{3-x}\text{V}_x\text{X}$ and their interaction with strong local moments of Fe(B) impurities may play an important role in the anomalous behavior of the resistivity and other transport properties and in the possible heavy-fermion character of some of these compounds.

ACKNOWLEDGMENTS

This work is supported by the US Department of Energy under contract W-31-109-ENG-38, including a subcontract to Northeastern University, the Polish Council of Science and Research through grant number 2-P302-10307, and the allocation of supercomputer time at the NERSC and the Northeastern University Advanced Scientific Computation Center (NU-ASCC). We thank NATO for a travel grant.

REFERENCES

- ¹ F. Heusler, Verh. Dtsch. phys. Ges. **5**, 219 (1903).
- ² M. Fallot, Ann. Phys. (Paris) **6**, 305 (1936).
- ³ A. Arrot and H. Sato, Phys. Rev. **114**, 1420 (1959).
- ⁴ A. Oleś, Acta Phys. Polonica **27**, 343 (1965).
- ⁵ G. Foex, J. Phys. Radium **9**, 37 (1938) .
- ⁶ R. Benoit, J. Chem. Phys. **52**, 119 (1955).
- ⁷ A.J. Bradley and A.H. Jay, Proc. Roy. Soc. (London) A **136**, 210 (1932).
- ⁸ R. Nathans, M.T. Pigott and C.G. Shull, J. Phys. Chem. Solids **6**, 38 (1958).
- ⁹ M.B. Stearns, Phys. Rev. **168**, 588 (1968).
- ¹⁰ J. Moss and P.J. Brown, J. Phys. F **2**, 358 (1972).
- ¹¹ P.J. Webster, J. Phys. Chem. Solids **32**, 1221 (1971).
- ¹² K.R.A. Ziebeck and P.J. Webster, J. Phys. Chem. Solids **35**, 1 (1974).
- ¹³ K.R.A. Ziebeck and P.J. Webster, Phil. Mag. **34**, 973 (1976).
- ¹⁴ V.A. Niculescu, T.J. Burch and J. I. Budnick, J. Magn. Magn. Mater. **39**, 223 (1983), and references therein.
- ¹⁵ R.A. de Groot, F.M. Mueller, P.G. van Engen and K.H.J. Buschow, Phys. Rev. Lett. **50**, 2024 (1983).
- ¹⁶ R.A. de Groot and K.H.J. Buschow, J. Magn. Magn. Mater. **54-57**, 1377 (1986).
- ¹⁷ S. Fujii, S. Sugimura, S. Ishida and S. Asano, J. Phys.: Condens. Matter **2**, 8583 (1990).
- ¹⁸ A. Bansil, S. Kaprzyk and J. Toboła, Applications of Multiple Scattering Theory in Material Science, MRS Symp. Proc. **253**, 505(1992).
- ¹⁹ S. Ishida, S. Fujii, S. Kashiwagi and S. Asano, J. Phys. Soc. Jpn. **64**, 2152 (1995).
- ²⁰ H. van Leuken and R.A. de Groot, Phys. Rev. Lett. **74**, 1171 (1995).
- ²¹ K. Endo, H. Matsuda, K. Ooiwa and K. Itoh, J. Phys. Soc. Jpn. **64**, 2329 (1995).
- ²² J. Pierre, R.V. Skolozdra, Y.K. Gorelenko and M. Kouacou, J. Magn. Magn. Mater. **134**, 95 (1994).
- ²³ M.A. Kouacou, J. Pierre and R.V. Skolozdra, J. Phys.: Condens. Matter **7**, 7373 (1995).
- ²⁴ J. Toboła, J. Pierre, S. Kaprzyk, R.V. Skolozdra and M.A. Kouacou, J. Magn. Magn. Mater. **159**, 192 (1996).
- ²⁵ H. Kronmüller, J. Magn. Magn. Mater. **140**, 25 (1996).
- ²⁶ Y. Nishino, M. Kato, S. Asano, K. Soda, M. Hayasaki and U. Mizutani, Phys. Rev. Lett. **79**, 1909 (1997).
- ²⁷ D.J. Singh and I.I. Mazin, Phys. Rev. **B 57**, 14 352 (1998).
- ²⁸ G.Y. Guo, G.A. Botton and Y. Nishino, J. Phys.: Condens. Matter **10**, L119 (1998).
- ²⁹ R. Weht and W.E. Pickett, Phys. Rev. **B 58**, 6855 (1998).
- ³⁰ N. Kawamiya, Y. Nishino, M. Matsuo and S. Asano, Phys. Rev. **B 44**, 12406 (1991).
- ³¹ Y. Nishino, S. Inoue, S. Asano and N. Kawamiya, Phys. Rev. **B 48**, 13607 (1993).
- ³² See, e.g., A.C. Switendick, Solid State Commun. **19**, 511 (1976).
- ³³ E.J.D. Garba and R.L. Jacobs, J. Phys. F **16**, 1485 (1986).
- ³⁴ S. Ishida, S. Fujii, N. Shinmura and S. Asano, J. Phys.: Condens. Matter **1**, 5115 (1989).
- ³⁵ S. Ishida, I. Ishida, S. Asano and J. Yamashita, J. Phys. Soc. Jpn. **41**, 1570 (1976).
- ³⁶ R. Haydock and M.V. You, Solid State Commun. **33**, 299, (1980).
- ³⁷ A.R. Williams, V.L. Moruzzi, C.D. Gelatt, J. Kübler and K. Schwartz, J. Appl. Phys. **53**, 2019 (1982).

- ³⁸ J. Kudrnovsky, N. E. Christensen and O. K. Andersen, Phys. Rev. **B 43**, 5924 (1991).
- ³⁹ T.J. Burch, J.I. Budnick, V.A. Niculescu, K. Raj and T. Litrenta, Phys. Rev. **B 24**, 3866 (1981), and references therein.
- ⁴⁰ T.J. Burch, C.A. Weiler, K. Ray, J.I. Budnick, V. Niculescu, G.C. Papaefthymiou and R.B. Frankel, J. Magn. Magn. Mater. **27**, 55 (1982).
- ⁴¹ S. Fujii, S. Ishida and S. Asano, J. Phys. Soc. Jpn. **63**, 1881 (1994).
- ⁴² N. Kawamiya and K. Adachi, Trans. Jpn. Inst. Met. **23**, 296 (1982).
- ⁴³ J.J. Jia, T.A. Callcott, W.L. O'Brien, Q.Y. Dong, D.R. Mueller, D.L. Ederer, Z. Tan and J.I. Budnick, Phys. Rev. **B 46**, 9446 (1992).
- ⁴⁴ S. Kaprzyk and A. Bansil, Phys. Rev. **B 42**, 7358 (1990).
- ⁴⁵ A. Bansil and S. Kaprzyk, Phys. Rev. **B 43**, 10335 (1991).
- ⁴⁶ For reviews of the KKR-CPA theory see Refs. 47–50 below, and references therein.
- ⁴⁷ A. Bansil, in *Electronic Band Structure and its Applications*, Lecture Note Series, Vol. 283, edited by M. Yussouff (Springer-Verlag, Heidelberg, 1987), p273.
- ⁴⁸ A. Bansil, in *Positron Annihilation*, edited by P. G. Coleman, S.G. Sharma, and L.M. Diana (North-Holland, Amsterdam, 1982), p291.
- ⁴⁹ H. Ehrenreich and L.M. Schwartz, Solid State Physics **31**, 149 (1976).
- ⁵⁰ G.M. Stocks and H. Winter, in *Electronic Structure of Complex Systems*, edited by P. Phariseau and W. Temmerman (Plenum, New York, 1984).
- ⁵¹ S. Kaprzyk and P.E. Mijnarends, J. Phys. C **19**, 1283 (1986).
- ⁵² A discussion of cases where more than one sublattice is disordered simultaneously is considered outside the scope of this work.
- ⁵³ A. Bansil, Z. Naturforschung **48a**, 165 (1993).
- ⁵⁴ S. Kaprzyk, Acta Phys. Polonica A **91**, 135 (1997).
- ⁵⁵ For properties considered in this article, only the ‘diagonal’ matrix elements of the Green function, where one stays within the central unit cell, are required. More general ‘off-diagonal’ matrix elements needed for computing, for example, momentum density, (cf. Refs. 56 and 57) are not considered in Eq. (2.1).
- ⁵⁶ P.E. Mijnarends and A. Bansil, Phys. Rev. **B 13**, 2381 (1976).
- ⁵⁷ A. Bansil, R.S. Rao, P.E. Mijnarends and L. Schwartz, Phys. Rev. **B 23**, 3608 (1981).
- ⁵⁸ B. Segall, Phys. Rev. **105**, 108 (1957).
- ⁵⁹ E. Muller-Hartman, Solid State Commun. **12**, 1269 (1973).
- ⁶⁰ F. Ducastelle, J. Phys. C **7**, 1795 (1974).
- ⁶¹ R. Mills and P. Ratanavararaksa, Phys. Rev. **B 18**, 5291 (1978).
- ⁶² Th. Kaplan, P.L. Leath, L.J. Gray and H.W. Diehl, Phys. Rev. **B 21**, 4230 (1980).
- ⁶³ X.-G. Zhang and W.H. Butler, Phys. Rev. **B 46**, 7433 (1992).
- ⁶⁴ N. Kawamiya and K. Adachi, J. Magn. Magn. Mater. **31-34**, 145 (1983).
- ⁶⁵ N. Kawamiya, K. Adachi and Y. Nakamura, J. Phys. Soc. Jpn. **33**, 1318 (1972).
- ⁶⁶ J. Waliszewski, L. Dobrzyński, A. Malinowski, D. Satuła, K. Szymański, W. Prandl, Th. Brückel and O. Schärpf, J. Magn. Magn. Mater. **132**, 349 (1994).
- ⁶⁷ U. von Barth and L. Hedin, J. Phys. C **5**, 1629 (1972).
- ⁶⁸ V.A. Niculescu, K. Raj, J. I. Budnick, T. J. Burch, W.A. Hines and A. H. Menotti, Phys. Rev. **B 14**, 4160 (1976).
- ⁶⁹ K. Motoya, S.M. Shapiro and Y. Muraoka, Phys. Rev. **B 28**, 6183 (1983).
- ⁷⁰ E. Popiel, M. Tuszyński, W. Zarek and T. Rendecki, J. Less Common Metals **146**, 127

- (1989).
- ⁷¹ K.H.J. Buschow and P.G. van Engen, J. Magn. Magn. Mater. **25**, 90 (1983).
- ⁷² S. Froyen, Phys. Rev. **B 39**, 3168 (1989).
- ⁷³ D.G. Pettifor, *Bonding and Structure of Molecules and Solids*, (Clarendon, Oxford, 1995), p. 191.
- ⁷⁴ P.S. Ho, G.W. Rubloff, J.E. Lewis, V.L. Moruzzi and A.R. Williams, Phys. Rev. **B 22**, 4784 (1980).
- ⁷⁵ The use of $\ell_{max} = 2$ on Si sites is thus important.
- ⁷⁶ A proper comparison between theory and experiment should involve matrix element effects. For this reason, differences in the relative intensities of the three peaks in Fig. 8 from those of Jia *et al.* are to be expected.
- ⁷⁷ For example, comparing the $x = 0.75$ and $x = 0.0$ Fe(B) results (Figs. 12b4 and 12b1) we see that the up-spin CDOS is much smoother for $x = 0.75$ even though this is hardly so for the down spins.
- ⁷⁸ J.I. Budnick, Z. Tan and D.M. Pease, Physica **B 158**, 31 (1989).
- ⁷⁹ V.L. Moruzzi, J.F. Janak and A.R. Williams, in *Calculated Electronic properties of Metals* (Pergamon, New York, 1978).
- ⁸⁰ J. Kübler, A.R. Williams and C.B. Sommers, Phys. Rev. **B 24**, 1745 (1983).
- ⁸¹ D.D. Johnson, D.M. Nicholson, F.J. Pinski, B.L. Gyorffy and G.M. Stocks, Phys. Rev. Lett. **56**, 2088 (1986).
- ⁸² However, care should be exercised in this respect since it is well-known that the local-density approximation (LDA) tends to underestimate the band gap in semiconductors.
- ⁸³ Z. Fisk, D.W. Hess, C.J. Pethick, D. Pines, J.L. Smith, J.D. Thompson and J.O. Willis, Science **239**, 33 (1988).
- ⁸⁴ S.J. Pickart and R.Nathans, Phys. Rev. **123**, 1163 (1961).
- ⁸⁵ A. Paoletti and L. Passari, Nuovo Cim. **32**, 25 (1964).
- ⁸⁶ W.A. Hines, A.H. Menotti, J.I. Budnick, T.J. Burch, T. Litrenta, V.A. Niculescu and K. Raj, Phys. Rev. **B 13**, 4060 (1976).
- ⁸⁷ M. Kawakami, Physica B **186-188**, 1037 (1993); J. Magn. Magn. Mater. **128**, 284 (1993);
- ⁸⁸ M. Kawakami, S. Uwanuyu, T. Nagano and T. Shinohara, J. Phys. Soc. Jpn. **64**, 4411 (1995); M. Kawakami, S. Nishizaki and T. Fujita, J. Phys. Soc. Jpn. **64**, 4081 (1995).
- ⁸⁹ M. Tuszyński, W. Zarek and E. Popiel, Hyperfine Interactions **59**, 369 (1990).

FIGURES

FIG. 1. Crystal structure of $\text{Fe}_{3-x}\text{V}_x\text{X}$. The four crystallographic positions, denoted by A-D, are shown by shadings of different intensity. The A and C sites are equivalent in the present case. Fe and V atoms occupy B sites, while Si, Ga, or Al atoms sit at D sites.

FIG. 2. Schematic diagram of the up- and-down spin component densities of states on Fe(A,C), Fe(B), and V(B) sites for a) Fe_3Si and b) Fe_2VSi . The horizontal dashed lines mark the Fermi levels for Fe_3Si and Fe_2VSi , the chain lines for the corresponding Ga and Al compounds. The kinks in the latter represent an overall shift of the entire set of down-spin bands. The tick marks on the energy axes denoted Fe(A,C), Fe(B), V, and Si(p) give the various on-site metal d and metalloid p energy levels. Tick marks denoted V in a) refer to the energy levels of a single V impurity in Fe_3X ; similarly Fe(B) in b) refers to single Fe(B) impurity levels in Fe_2VX .

FIG. 3. Schematic representation of the common-band model of bonding in a binary AB system. a) Densities of states of solids A and B before alloying; b) component densities of states in the alloy AB; c) total density of states in the alloy AB. W denotes the width of the common band, W_{AB} the bandwidth after bonding. The quantities E_A^0 and E_B^0 give the free-atom energy levels while E_A and E_B denote the local on-site energy levels. After Ref. 73.

FIG. 4. Computed total magnetic moment (per Wigner-Seitz cell) and the moments per atom on various inequivalent sites in $\text{Fe}_{3-x}\text{V}_x\text{Si}$ as a function of V concentration x . All values given in units of Bohr magnetons (μ_B). Different symbols are explained in the legend. Lines are drawn through the theoretical points to guide the eye. Experimental points (open circles) for the total moment are after Ref. 14.

FIG. 5. Same as Fig.4, except that this figure refers to $\text{Fe}_{3-x}\text{V}_x\text{Ga}$. Experimental points after Ref. 64.

FIG. 6. Same as Fig.4, except that this figure refers to $\text{Fe}_{3-x}\text{V}_x\text{Al}$. Experimental points after Refs. 70 and 89.

FIG. 7. Component density of states (CDOS) for various inequivalent sites in Fe_3Si (topmost row). Different angular momentum contributions to the CDOS are shown. The majority (up) and minority (down) spin part of the CDOS is given in each case. The dotted vertical lines mark the Fermi energy (E_F). Note different scales.

FIG. 8. Computed partial density of states in the s and d channels associated with a Si site in Fe_3Si ; the spectrum has been convoluted with a Gaussian of 2.0 eV (full-width-at-half-maximum) to mimic experimental broadening of the soft x-ray emission spectra of Ref. 43.

FIG. 9. Total and site-decomposed density of states in Fe_3Si , Fe_3Ga , and Fe_3Al . See caption to Fig.7 for other details.

FIG. 10. Same as Fig.9, except that this figure refers to Fe_2VX alloys.

FIG. 11. Dispersion curves along high symmetry lines in the Brillouin zone in ferromagnetic Fe_2VSi (upper) and paramagnetic Fe_2VGa (lower). The darker and lighter curves in the upper picture represent spin-up and spin-down bands in Fe_2VSi respectively. The Fermi energy is marked by horizontal lines.

FIG. 12. Site-dependent density of states in $\text{Fe}_{3-x}\text{V}_x\text{Si}$ at Fe(A,C), Fe(B), and V(B) sites for each spin direction as a function of the V concentration x . The Fermi energy is marked by dotted vertical lines.

FIG. 13. Total up- and down-spin density of states in $\text{Fe}_{3-x}\text{V}_x\text{Si}$, $\text{Fe}_{3-x}\text{V}_x\text{Ga}$, and $\text{Fe}_{3-x}\text{V}_x\text{Al}$ for different V concentrations x . The Fermi energies are marked by dotted vertical lines.

FIG. 14. Same as Fig.12, except that this figure refers to $\text{Fe}_{3-x}\text{V}_x\text{Ga}$.

FIG. 15. The differences between the total energies of $\text{Fe}_{3-x}\text{V}_x\text{Si}$ and constituent atoms with V in the B sublattice (solid curve) and V in the A or C sublattices (dashed curve).

TABLES

TABLE I. The lattice parameters (a) and the muffin-tin radii (S_k) in Fe_3X .

	$a(\text{\AA})$	$S_k(\text{\AA})$
Fe_3Si	5.653 ^a	1.224
Fe_3Ga	5.812 ^b	1.258
Fe_3Al	5.791 ^c	1.254

^aRef. 68.

^bRef. 42.

^cRef. 69.

TABLE II. Magnetic moments on various inequivalent sites in the end compounds Fe_3X and Fe_2VX in units of Bohr magnetons (μ_B). The results of the present computations are given together with those of a number of other computations and relevant experiments. The values of moments for a single V(B) impurity in Fe_3X and a single Fe(B) impurity in Fe_2VX are based on our KKR-CPA computations in the limiting compounds, and are marked with stars.

	Fe(A,C)			Fe(B)			V(B)	X(D)		Total	
	Theory present	others	Exp.	Theory present	others	Exp.	Theory present	Theory present	others	Theory present	others
Fe_3Si	1.34	1.2 ^a 1.10 ^c	1.2 ^b 1.07 ^d 1.35 ^e	2.52	1.9 ^a 2.52 ^c	2.4 ^b 2.23 ^d 2.20 ^e	-0.62*	-0.08	-0.08 ^d	5.07	4.63 ^d
Fe_3Ga	1.87	2.09 ^f	1.7 ^g	2.47	2.38 ^f	2.5 ^g	-1.16*	-0.08	-0.10 ^f	6.01	
Fe_3Al	1.90	1.36 ^h 1.26 ⁱ 1.89 ^j 1.9 ^k	1.5 ^b	2.44	2.48 ^h 2.16 ⁱ 2.34 ^j 2.4 ^k	2.18 ^b	-1.27*	-0.10	-0.14 ^j	6.03	
Fe_2VSi	0.43	0.37 ^c		3.08*			-0.11	-0.02	-0.02 ^c	0.68	0.70 ^c
Fe_2VGa	0.03			3.20*			-0.06	0.00		0.00	
Fe_2VAl	0.03			3.18*			-0.04	0.00		0.00	

^aRef. 33.

^bRef. 84,85.

^cRef. 38.

^dRef. 10.

^eRef. 86.

^fRef. 34.

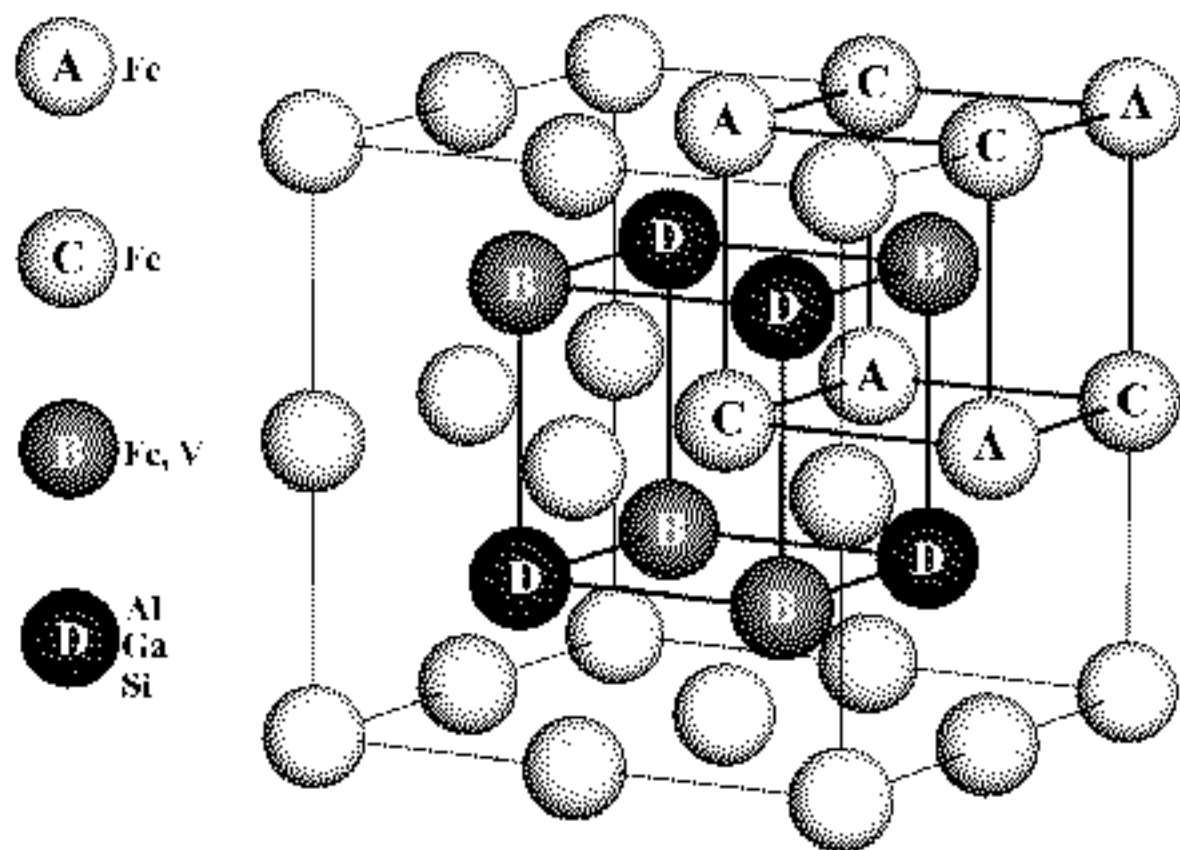
^gRef. 42.

^hRef. 37.

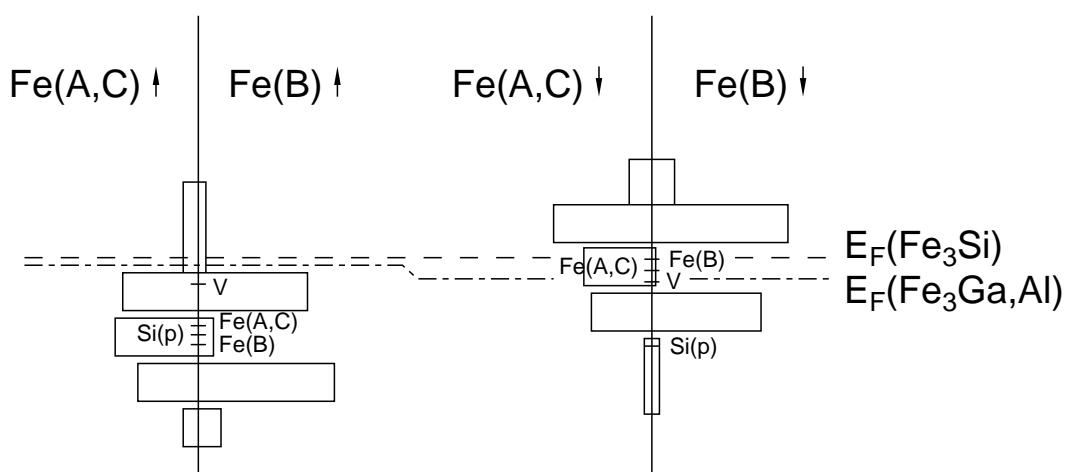
ⁱRef. 35.

^jRef. 28.

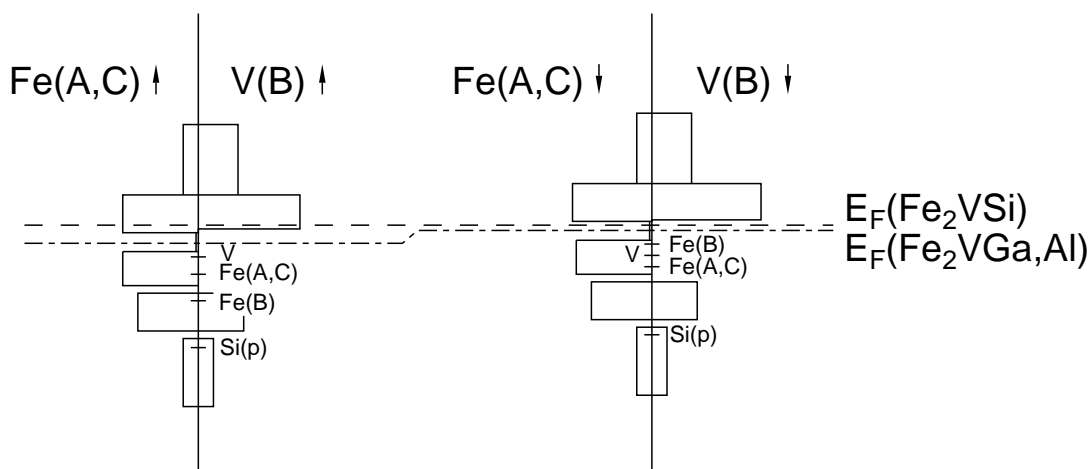
^kRef. 27.

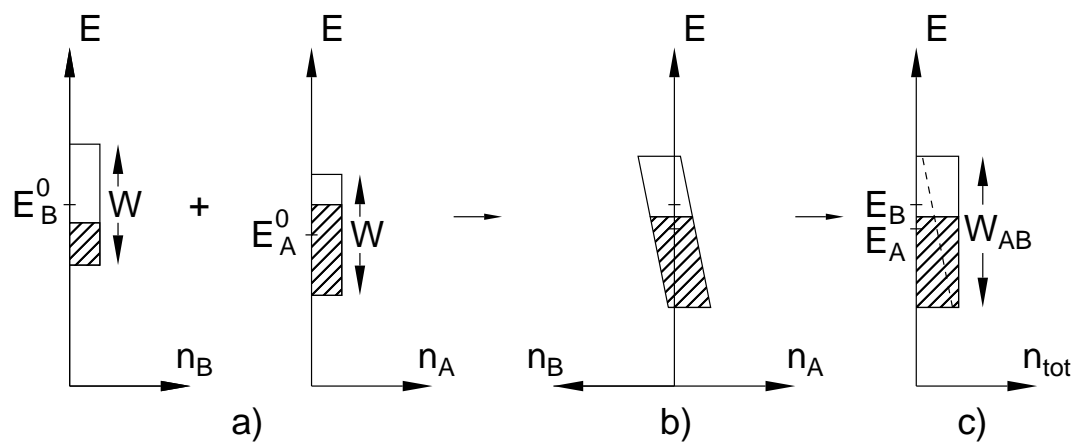


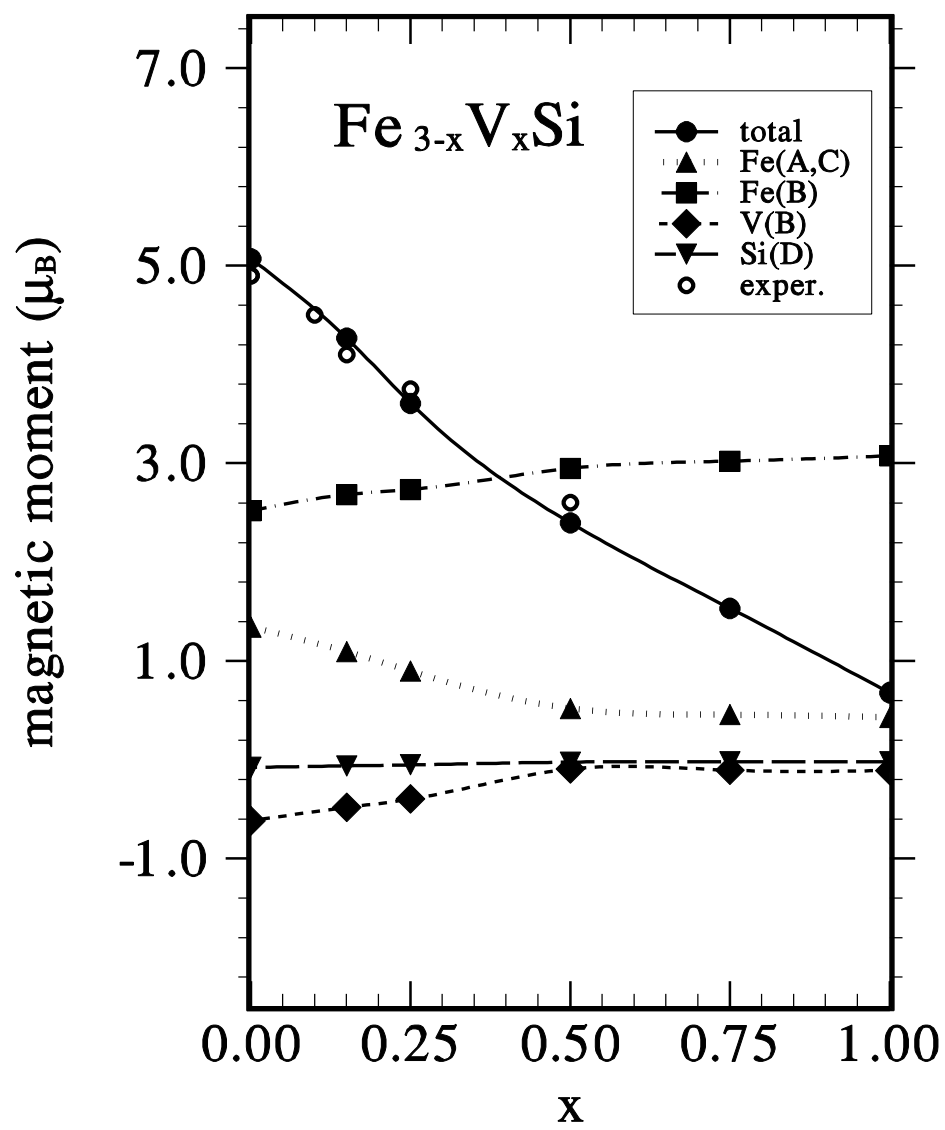
a) Fe_3X

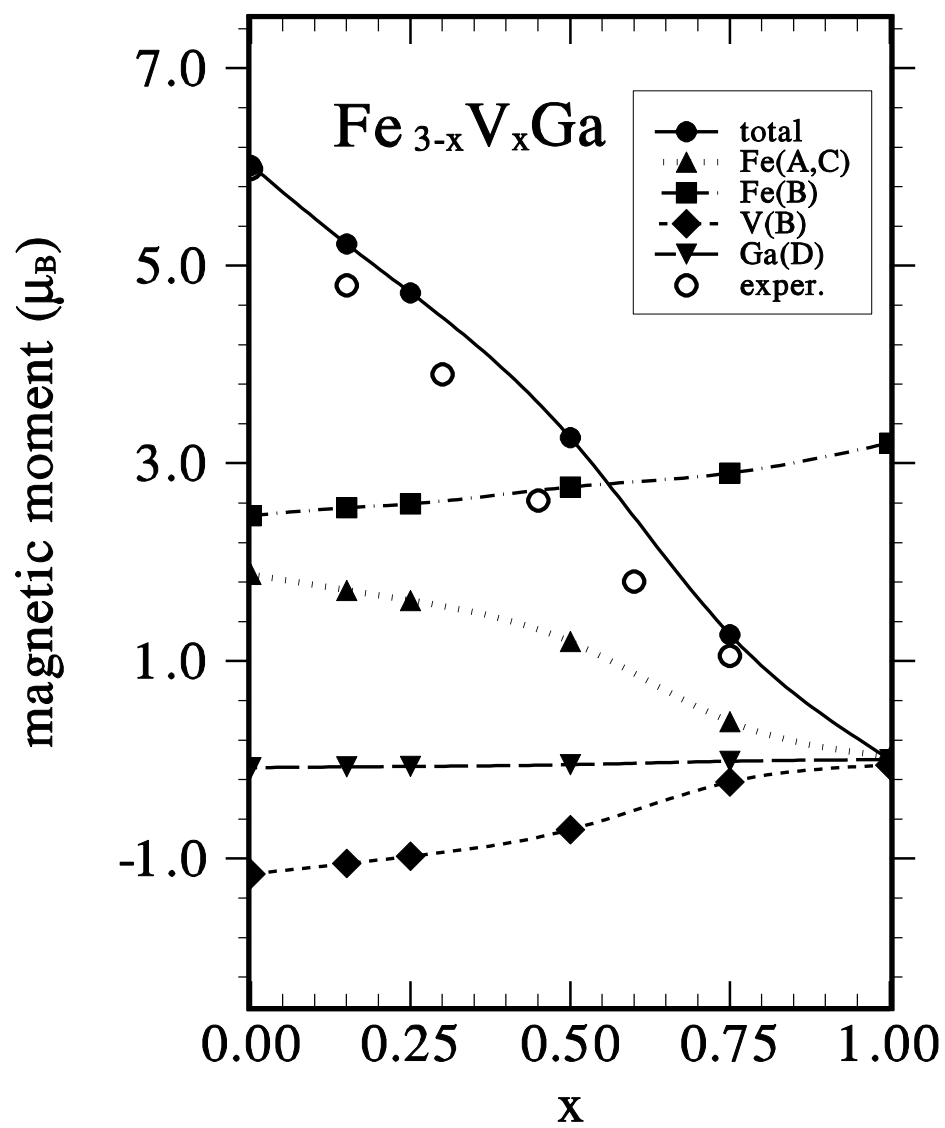


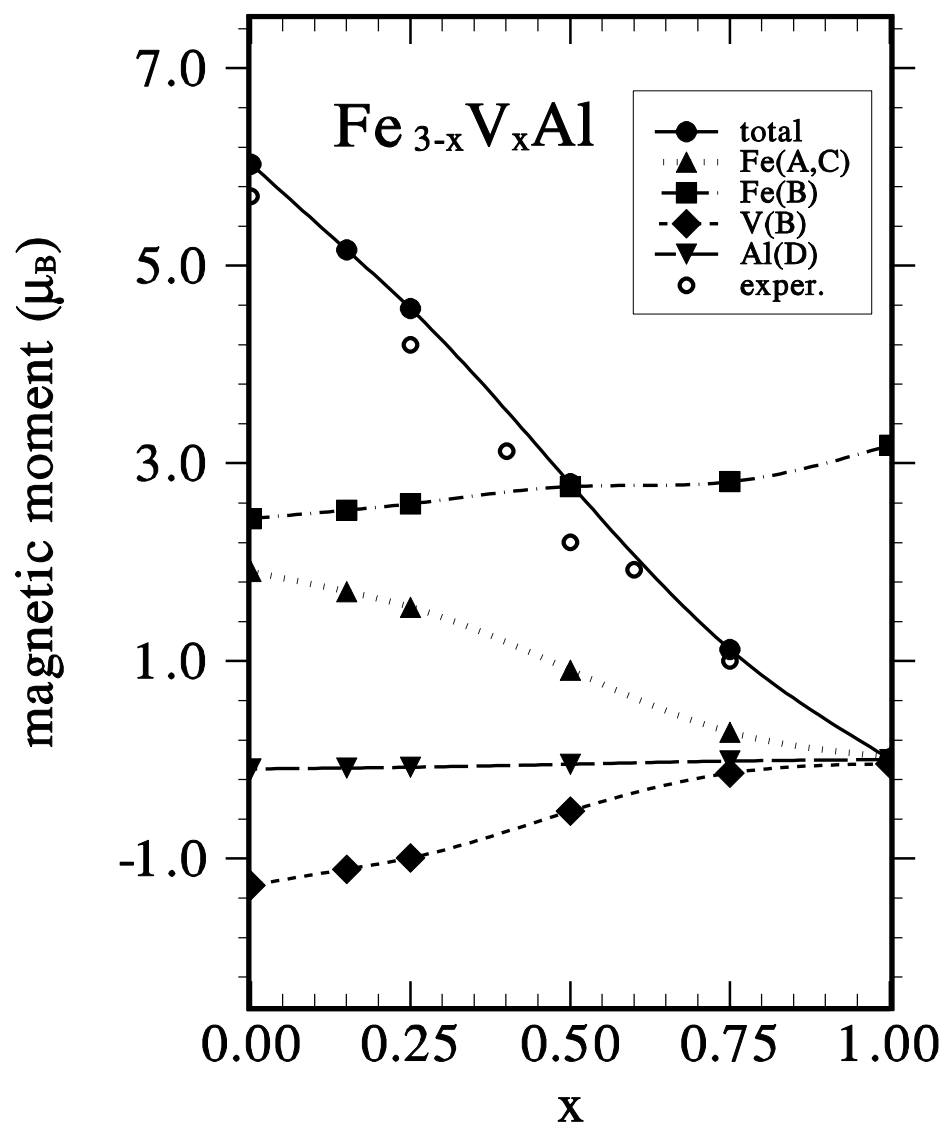
b) Fe_2VX



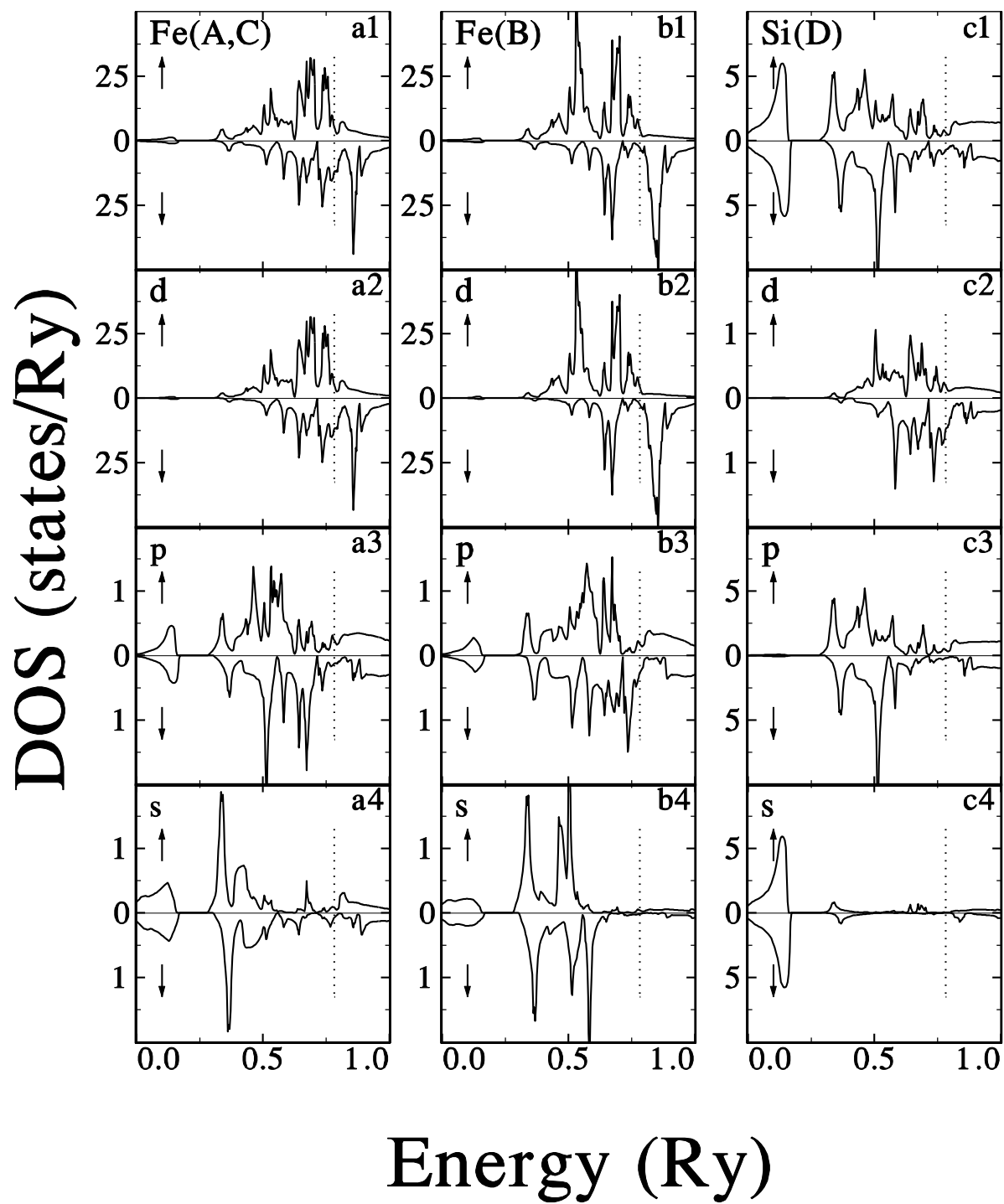


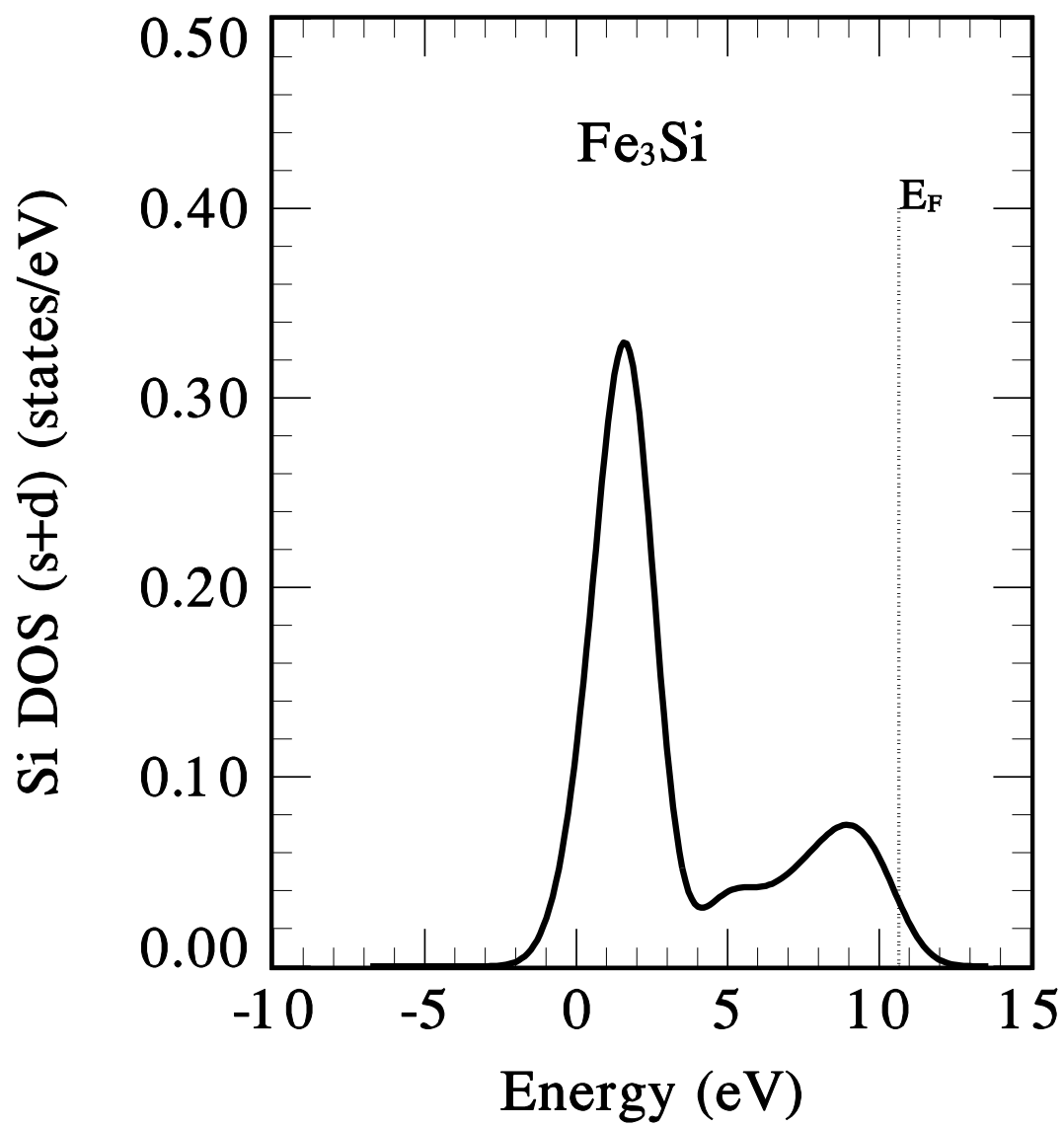






Fe_3Si

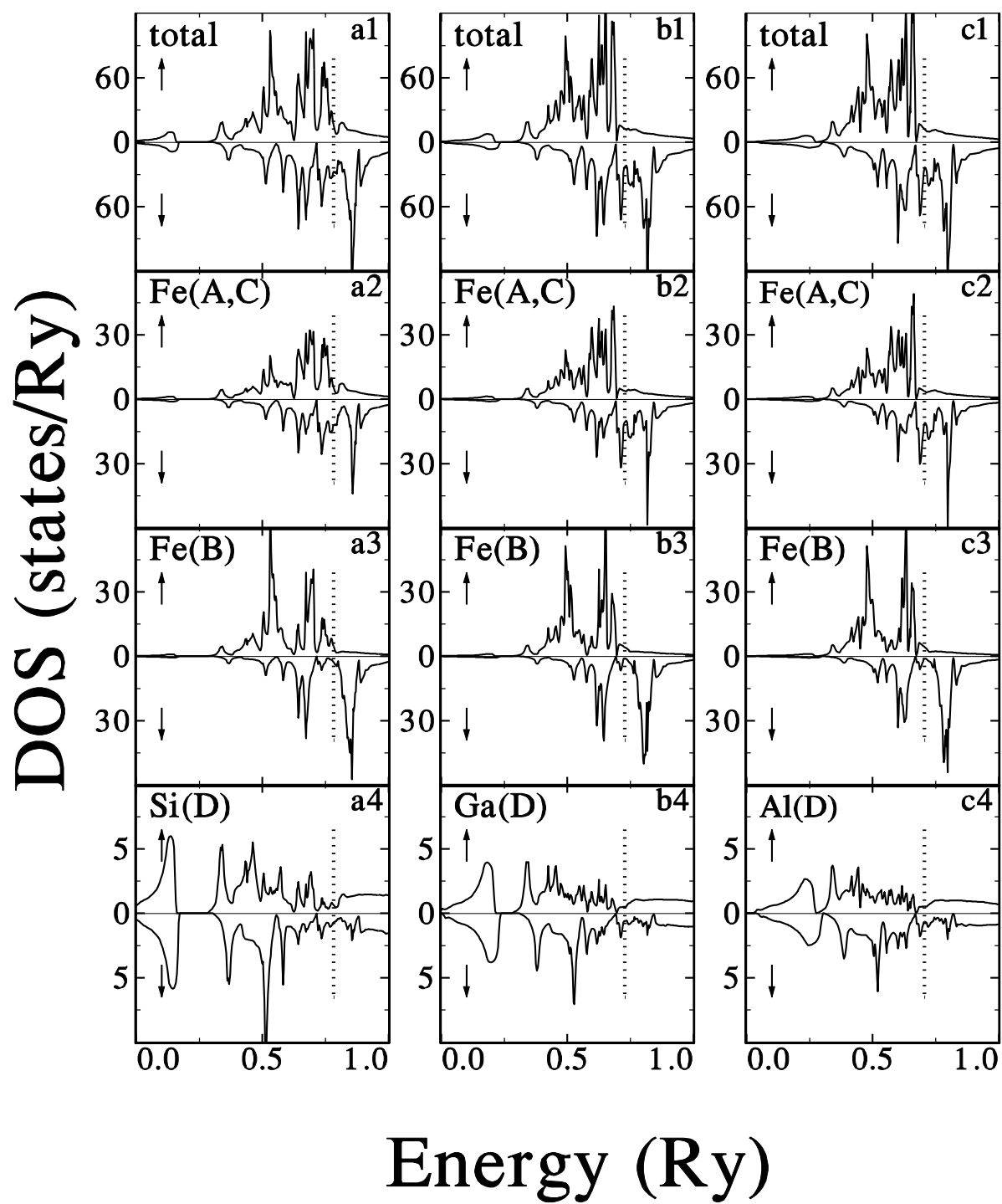




Fe_3Si

Fe_3Ga

Fe_3Al



Fe_2VSi

Fe_2VGa

Fe_2VAl

